BRNO UNIVERSITY OF TECHNOLOGY
VYSOKÉ UČENÍ TECHNICKÉ V BRNĚ

FACULTY OF ELECTRICAL ENGINEERING AND COMMUNICATION
FAKULTA ELEKTROTECHNIKY
A KOMUNIKAČNÍCH TECHNOLOGIÍ

DEPARTMENT OF BIOMEDICAL ENGINEERING
ÚSTAV BIOMEDICÍNSKÉHO INŽENÝRSTVÍ

CORRECTION OF IMAGE DISTORTION OF MICROSCOPIC SCENE
KOREKCE DISTORZE OBRAZU MIKROSKOPICKÉ SCÉNY

MASTER'S THESIS
DIPLOMOVÁ PRÁCE

AUTHOR
AUTOR PRÁCE
Bc. Kristýna Temelová

SUPERVISOR
VEDOUCÍ PRÁCE
Ing. Jan Odstrčilík, Ph.D.

BRNO 2016

BRNO UNIVERSITY OF TECHNOLOGY

Faculty of Electrical Engineering and Communication

Department of Biomedical Engineering

Diploma thesis

Master's study field

Biomedical Engineering and Bioinformatics

Student: Bc. Kristýna Temelová
Year of study: 2

ID: 146206
Academic year: 2015/16

TITLE OF THESIS:

Correction of image distortion of microscopic scene

INSTRUCTION:

1) Perform a literature research in the field of correction of image distortion and image registration. Focus on the crystalline structure images from the transmission electron microscope (TEM) and describe optical aberrations of this system. 2) Propose an optimal method of fitting the model of crystal lattice with its real image coming from TEM. Define the applicability of this method for correction of distortion. 3) Implement a software solution of the chosen method in MATLAB. Test the method on simulated data. 4) Use the algorithm on real images of atomic structure of Gold with known lattice constant. Test the algorithm also on partially degraded images. 5) Discuss the results and evaluate efficiency and applicability of the method. The work is realized with the cooperation of FEI Czech Republic company which provides the data for analysis.

REFERENCE:

[1] JAN, J. Medical image processing, reconstruction and restoration: concepts and methods. Boca Raton: Taylor & Francis. 2006, ISBN 0-8247-5849-8, 730 s.
[2] HAJNAL, J. V., et al. Medical image registration. Boca Raton: CRC Press. 2001, ISBN 08-493-0064-9, 382 s.
[3] WILLIAMS, D. B., et al. Transmission electron microscopy: a textbook for materials science. Springer US. 2009, ISBN 978-0-387-76500-6, 775 s.

Assigment deadline: 8. 2. 2016 ***Submission deadline:*** 20. 5. 2016

Head of thesis: Ing. Jan Odstrčilík, Ph.D.
Consultant: Ing. Miloš Malínský, Ph.D.

prof. Ing. Ivo Provazník, Ph.D.
Subject Council chairman

WARNING:

ABSTRACT

This diploma thesis describes a method of using image registration to correct geometrical distortions of images of regular crystalline structures acquired by a transmission electron microscope (TEM). The aim of this work is to create an algorithm in Matlab that can correct these distortions through finding a spatial transformation deforming the distorted image in order to fit it to its model grid. The transformation is searched with help of the optimization methods optimizing the chosen criterion function.

KEYWORDS

TEM, correction of distortion, image registration, optimization, crystalline structures

ABSTRAKT

Tato diplomová práce popisuje metodu využití lícování obrazů pro korekci geometrické distorze obrazů pravidelných krystalických struktur získaných z transmisního elektronového mikroskopu (TEM). Cílem této práce je vytvořit algoritmus v Matlabu, který dokáže tyto vady eliminovat nalezením prostorové transformace, která nalícuje zkreslený obraz na jeho modelovou mřížku. Transformace je hledána s využitím optimalizačních metod, které optimalizují zvolenou kriteriální funkci.

KLÍČOVÁ SLOVA

TEM, korekce distorze, lícování obrazů, optimalizace, krystalické struktury

TEMELOVÁ, K. *Correction of image distortion of microscopic scene*. Brno: Brno University of Technology, Faculty of Electrical Engineering and Communication, Departement of Biomedical Engineering 2016. 82 p. Supervisor of diploma thesis Ing. Jan Odstrčilík, Ph.D.

DECLARATION

I declare that I have elaborated my diploma thesis on the theme of "Correction of image distortion of microscopic scene" independently, under the supervision of the diploma thesis supervisor and with the use of technical literature and other sources of information which are all quoted in the thesis and detailed in the list of literature at the end of the thesis.

As the author of the diploma thesis I furthermore declare that, concerning the creation of this diploma thesis, I have not infringed any copyright. In particular, I have not unlawfully encroached on anyone's personal copyright and I am fully aware of the consequences in the case of breaking Regulation § 11 and the following of the Copyright Act No 121/2000 Vol., including the possible consequences of criminal law resulted from Regulation § 152 of Criminal Act No 140/1961 Vol.

Brno ....

(author's signature)

ACKNOWLEDGEMENT

I would like to thank my supervisor Ing. Jan Odstrčilík, Ph.D. and my consultant Ing. Miloš Malínský, Ph.D. for the professional advice and kind and valuable help during the elaboration of my diploma thesis. I would also thank Ing. Ondřej Sháněl, Ph.D., the idea creator of the theme of this thesis, for all the valuable advice. My special thanks belong to my family, friends and to my boyfriend Ondra for the patient support during all my university studies.

Brno ....

(author's signature)

CONTENT

A LIST OF FIGURES

INTRODUCTION

An image from a Transmission Electron Microscope (TEM) is always affected by optical aberrations. To minimize these aberrations, many hardware correction elements (multipole correctors, deflection coils, stigmators) are present in the TEM. Furthermore, the demands on precise manufaturing of some components are extremely high. Nowadays, in the time of information technologies, a software solution would be appreciated.

The aim of this work is to use image registration techniques to correct the geometrical distortion of images acquired by a TEM. The main images to be processed in this work are the images of gold with a regular crystalline structure. This work looks for an algorithm of model based image registration method that deforms the real image from TEM according to atomic features of a model grid of the processed specimen. The algorithm considers geometrical distortion controlled over specific deformation properties of a 3^{rd} order polynomial. Higher order polynomial coefficients won't be part of this work. The main task of this work is to find an optimal combination of a criterion function and an optimization method suitable for this specific problem.

The theoretical part of this work includes a literature research relevant to the task. The first chapter is about the TEM, the reason of use, its construction, operating modes, image formation and crystalline specimens. The second chapter summarizes the optical aberrations of the TEM with the accent on the geometrical distortion. The third chapter comprises the State of the Art summarizing some methods utilized for the correction of distortion and strain measurement. The fourth chapter presents the image registration theory, the geometrical transformaions and the optimization methods.

The practical part comprises a design of an algorithm for the correction of distortion in Matlab interface. The fifth chapter describes the proposed method, the sixth chapter describes testing on simulated data, the seventh chapter presents the results of testing on real data and the folowing discussion evaluates the results.

1 TRANSMISSION ELECTRON MICROSCOPE

A Transmission Electron Microscope (TEM) uses electrons passing through a sufficiently thin specimen to create an image. A TEM typically provides a magnification in the range of 10^3 to 10^6 with resolution greater than 0.1 nm and is utilized both for the Life Science and the Material Science.

1.1 Why electrons

In 1924 Louis-Victor de Broglie formulated his hypothesis about the wave character of a particle. The wavelength λ is proportional to the Planck constant *h*, and inversely proportional to the momentum *p* ($p = mv$), as follows:

$$\lambda = \frac{h}{p} = \frac{h}{m \cdot v} \tag{1}$$

The electrons are negatively charged particles (with charge *e* and weight *m*) that can easily be accelerated by an electrical potential *U* which gives them a kinetic energy E_k. The obtained kinetic energy (for non-relativistic speeds) can be expressed like:

$$e \cdot U = \frac{1}{2} \cdot m \cdot v^2 \tag{2}$$

The wavelength λ can be expressed with the relation below. The first expression is suitable for relativistic speeds of the electron (close to the speed of light *c*), where the relativistic correction of mass should be applied, and the second expression is an approximation for standard use (for lower speeds).

$$\lambda = \frac{h}{\sqrt{2 \cdot m_0 \cdot e \cdot U \cdot (1 + \frac{e \cdot U}{2 \cdot m_0 \cdot c})}} \approx \frac{h}{\sqrt{2 \cdot m_0 \cdot e \cdot U}} \tag{3}$$

The maximum possible resolution *d* reachable by TEM is proportional to the wavelength λ of the electrons and inversely proportional to the numerical aperture *NA* (which depends on the semi-convergence angle *α*):

$$d = \frac{\lambda}{2 \cdot n \cdot sin(\alpha)} = \frac{\lambda}{2 \cdot NA} \tag{4}$$

So it is the reason why the electrons are used – the more they are accelerated by *U*, the more their wavelength λ decreases and so does the distance *d* of two resolved points [1].

1.2 TEM construction

The general scheme of a TEM is in *Figure 1*. The description of the functional blocks of TEM is in the following sub-chapters.

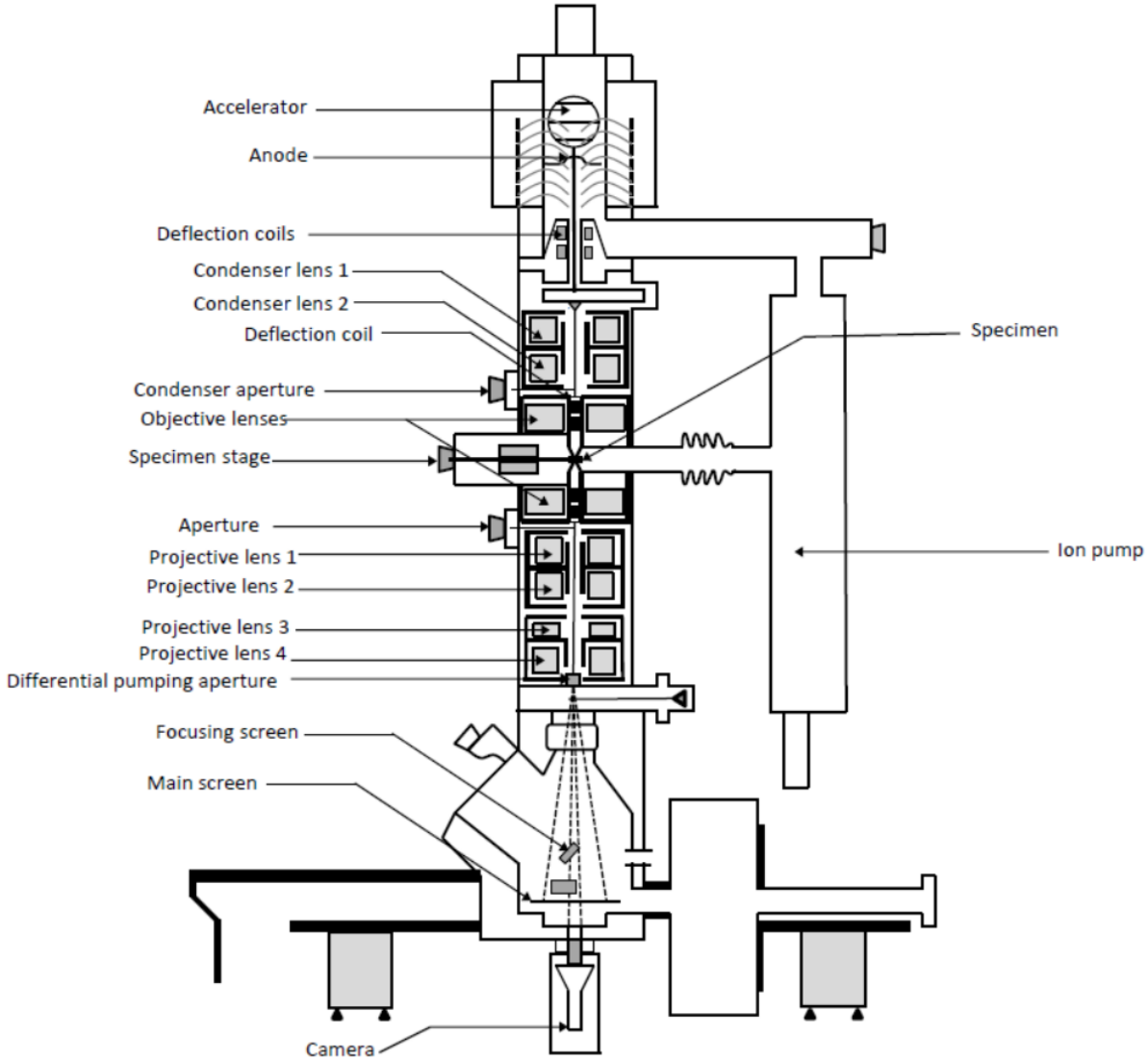

Figure 1: The TEM scheme [2]

- **Electron gun**

The electron gun serves for the production of electrons. They are generated from the cathode with high negative potential, emitted to the vacuum and accelerated to the anode plate. There are mainly two types of the electron sources – the **thermionic emission** and the **autoemision (field emission).** The autoemission can be furthermore divided into a Schottky emission (ZrO/W) and the cold field emission (W) [3], [4].

The **thermionic emission** works due to heating of the emitter to a high temperature - around 2700 K for the tungsten (W) hairpin filament and around 1400-2000 K for pointed lanthanum hexaboride (LaB_6) rod, which leads to the electrons leaping over the potential barrier with their thermal energy. The amount of emission from the tip of the cathode is controlled by a negatively biased Wehnelt cylinder.

The **Schottky emission** (or thermal-assisted field emitter) uses an application of electrostatic field which decreases the potential barrier restraining the electrons in the cathode and increases the emission current. The cathode is heated to about 1800 K, which helps electrons overcome the remaining potential barrier with their thermal energy. The heating helps also to prevent the adsorption of gas molecules. The cathode is commonly a V-shaped filament coated with ZrO with sharpened crystalline W tip at the end.

The **cold field emission** means tunneling of electrons through the potential barrier (they don't leap over) from the tungsten tip. The effect is induced by a sufficiently strong electrostatic field. The cold field emission is operating at a room temperature (300 K) [3], [4].

- ## Electron acceleration

The electrons can reach their final kinetic energy by an accelerating system creating a potential difference between the cathode and anode. The accelerating voltage in TEM is in the range from 60 to 300 kV [3].

- ## Condenser-lens system

The condenser-lens system is a part of illumination system (besides the gun module) that illuminates the specimen. There are two condenser lenses in the area above the specimen. The first one (C1) is a strong magnetic lens (has a small gap between the pole pieces) and serves for the spot size adjustment; the second one (C2) is a weak magnetic lens (the gap between the pole pieces is larger) and serves for change of the area of illumination [4].

- ## The objective lens and the specimen stage

The objective lens is the strongest lens in the microscope and is physically divided into two coils (the upper and lower objective lens). The specimen is inserted into the magnetic gap between the lenses through an airlock (a small evacuated chamber preventing contamination). The specimen must be very thin, which requires special preparation techniques. The specimen can be manipulated in *x*, *y* and *z* direction using the specimen holders. The electron beam is interacting with the specimen and the transmitted electrons contribute on the image formation.

The upper objective lens also contains a mini-condenser module which can be used for switching between micro- and nano-mode imaging [4].

- ## Projection system

The projection system is composed of a series of four magnetic lenses that are used mainly for the transfer and the final magnification of image. There is a weak diffraction lens (D), a strong intermediate lens (I) and two projection lenses (P1 – weak) and (P2 – strong). With cooperation of these four lenses, it is possible to set various magnification modes [4].

- ## Deflectors

The deflection coils serve for aligning the optical axes between individual modules of microscope. It is more effective way than trying to align these axes mechanically. There are in total three sets of deflectors. **Gun deflectors** are placed below the electron gun and serve for correcting the trajectory of the electron beam between the emitter and the illumination system. **Beam deflectors** are placed above the upper objective pole and serve for correcting the trajectory between the illumination system and the objective and **image deflectors** below the lower objective pole serve for aligning the objective and projective optical axes [4].

- ## Stigmators

The stigmator coils are used for changing the shape of the electron beam and correcting the 2-fold and 3-fold astigmatism. There are three sets of stigmators (**condenser**, **image** and **diffraction**) [2], [4].

- ## Apertures

The main apertures in the TEM are C1 and C2, OBJ and SA (selection area) [4]. They are generally used for controlling the electron beam (C1), controlling the convergence angle (C2), choosing the diffraction maxima (OBJ) and choosing the area on image plane for displaying the diffraction (SA).

- ## Vacuum system

The vacuum in the inner space of the microscope is necessary to prevent the random collisions of the accelerated electrons and air molecules which would result in the changes of energies and movement direction. It prevents also the contamination of the specimen by O_2, N_2 and CO_2 molecules. The pressure in the **gun space** is around $\mathbf{10^{-4} – 10^{-8}}$ **Pa** (pumped by an ion pump, depending on the emission principle), the pressure in the **specimen and column**

space is around $\mathbf{10^{-4}\text{-}10^{-5}}$ **Pa** (pumped also by an ion pump) and the pressure in the **imaging chamber** is about $\mathbf{10^{-3}\text{-}10^{-4}}$ **Pa** (pumped by an oil diffusion or turbo-molecular pump) [1], [3].

- **Screen, camera and computer**

The electrons finally reach the fluorescent screen, camera or STEM detector (used for scanning transmission electron microscopy) from where the image is converted into a digital output that can be displayed on the PC's monitor.

1.3 Crystalline specimens for TEM

The TEM specimens must be very thin (in range 10 nm to 100 nm): They contain almost no water. In case of anorganic crystalline samples, the sample thickness is reduced using mechanical, chemical, electrochemical or ion beam thinning [3].

Crystalline inorganic samples are composed of repeating unit cells forming a regular 3D structure characteristic for the material. The spacings and angles between the atoms in the unit cells are defined as the lattice parameters. There are many different crystallographic structures containing various atomic planes. To properly interpret the image created in TEM, it is necessary to define a marking system of the atomic rows, columns and planes orientation relative to the incident electron beam. This is specified by **Miller indices** [4].

Miller indices are used for the specification of the **directions** and **planes** in lattices or crystals. For a 2D lattice, there are 2 corresponding indices and for 3D lattice, there are 3 corresponding indices. This notation is very important in the Material Science because it influences the optical properties, dislocations in material, reactivity, etc [5].

Notation:

- (h,k,l) represents a point
- [hkl] represents a direction
- (hkl) represents a plane

Generally, a 3D plane is given by a linear combination of base vectors $\vec{a}$, $\vec{b}$ and $\vec{c}$. The vector $\vec{r}$ passing from the origin to the point in the lattice is defined as:

$$\vec{r} = r_1\vec{a} + r_2\vec{b} + r_3\vec{c}, \tag{5}$$

where (r_1, r_2, r_3) are the Miller indices. A negative number is denoted with a bar on top of the number: e.g. $\bar{1}$. The exqmple of use for 2D plane is on *Figure 2* [5].

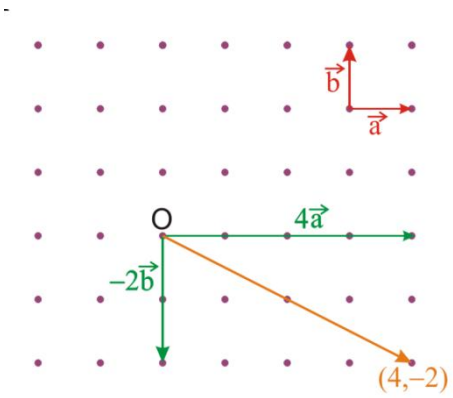

Miller indices for direction:

$[4\bar{2}]$

Figure 2: Miller indices $[4\bar{2}]$ for direction in 2D plane (for yellow vector) [5]

For orthogonal structures, the Miller indices represent the coordinates of the normal vector to the given plane. The indices evaluation is done by identification of intersections of planes with the base axes and expression of the reciprocal values [5]. The principle is demonstrated in *Figure 3*: the red (front) plane is parallel along *y* and *z* axes, but it intersects the *x* axis at the blue cross (distance 1) – the plane is then $(1\ \infty\ \infty)$; and the reciprocal values are $\left(\frac{1}{1}\ \frac{1}{\infty}\ \frac{1}{\infty}\right) = (100)$. *Remark:* if the intersections are $\left(\frac{1}{2}1\ 0\right)$, the Miller indices would be (210).

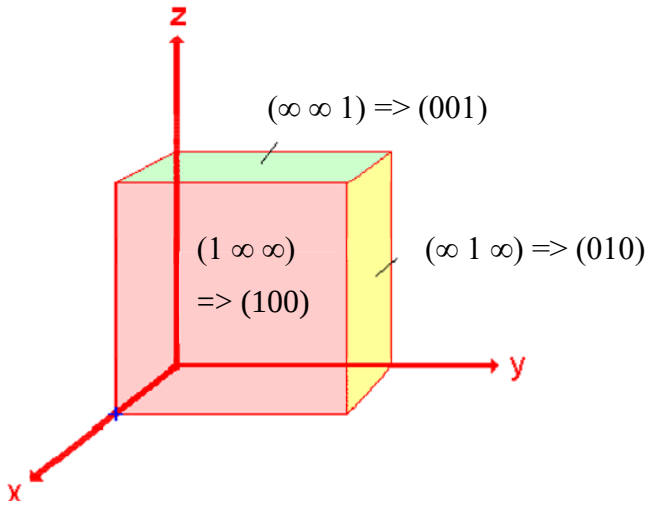

Figure 3: Miller indices for planes (in 3D) [5]

1.4 Image formation

For TEM image, it is essential that most of the electrons from the incident electron beam pass through the thin specimen and that almost no electrons are absorbed. The image contrast comes from the fact that some parts of the electron beam are scattered when interacting with the specimen (their direction change) and some are not. The trajectories of the electrons are changed mainly because of the Coulomb interactions of the charged particles. For the image creation, a part of the scattered electron beam can be excluded by the objective aperture. Thus, different images can be observed. Each of the observation mode (BF, DF, HREM) can be simultaneously affected by different contrast types [3], [4].

- **Mass-thickness contrast**

The scattering is affected mainly by two factors: the **sample thickness** and the **atomic number (Z)** of the material. The principle is the same. The thicker the specimen (or the higher the atomic number), the more the incident electrons will be scattered and less pass through the sample to the screen. This results in lower brightness in BF imaging. The mass-thickness contrast asi related primarily to the amorphous materials [3].

- **Diffraction contrast**

The diffraction contrast is applicable only to the crystalline samples and it can also participate on BF or DF image formation. The electrons are reflected from the different layers of sample in phase only if the **Bragg condition** is satisfied (here approximation for the first-order diffraction and a small Bragg-angle):

$$\lambda \approx \theta \cdot d, \tag{6}$$

where λ is the wavelength of the electron wave, d is the spacing between the atomic planes and θ is the deflection angle (angle of scattering) [4]. The bright points (Bragg spots) are formed in the diffraction pattern.

The diffraction contrast can be displayed after choosing one diffraction maximum by the objective aperture in the diffraction pattern (*Figure 5*). The image will be created mainly by the electrons scattered (diffracted) to one specific angle, so the image will be characteristic for the atomic planes with d corresponding to the Bragg condition (or for all planes with the same orientation) [4].

- **Phase contrast**

The phase contrast arises from the interference of a primary non-scattered electron wave with a wave that is phase-shifted due to specimen interaction (and objective lens aberrations). It is used for HREM / HRTEM (high resolution (transmission) electron microscopy) imaging of thin, mostly amorphous specimens. A large objective aperture or no aperture is used [3], [4].

Figure 4 represents three methods (bright field - BF, dark field - DF and HREM) how to use the objective aperture in order to create different images. The BF and DF images are both formed with help of the mass-thickness and diffraction contrast. The HREM image is formed with help of the phase contrast.

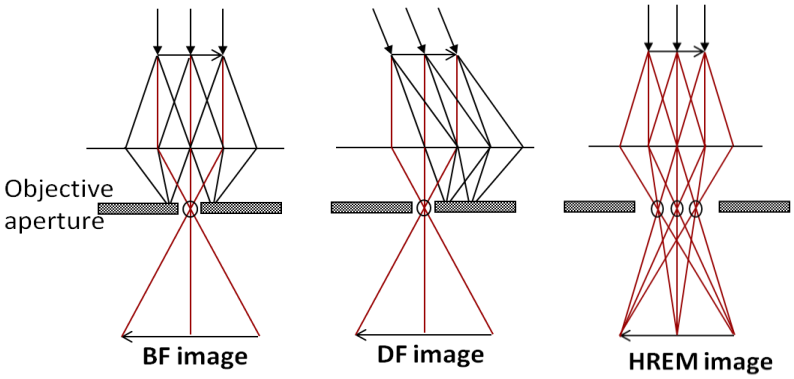

Figure 4: Imaging modes: BF, DF and HREM [6]

- **Diffraction**

The diffraction is always created together with image, but to visualize it, it is necessary to display the objective back focal plane (where the objective aperture is placed) instead of the image plane (where the SA aperture is placed). The view can be switched by refocusing the diffraction lens. *Figure 5* shows the diffraction pattern of a monocrystalline sample with atomic plane direction *[100]* producing single spots and a polycrystalline sample producing concentric circles where each represents an atomic plane [7].

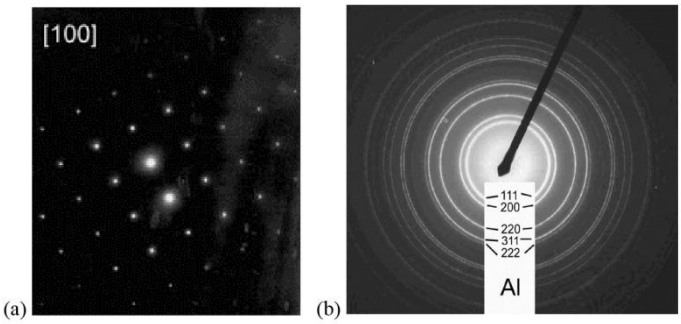

Figure 5: a) Diffraction pattern of a monocrystal and b) a polycrystal [7]

2 OPTICAL ABERRATIONS

The electromagnetic lenses of the electron microscope cause, like in the case of an optical microscope, some optical aberrations which lead to the creation of a distorted image and a reduced resolution. These aberrations cannot be overlooked in case of high resolution applications HR(S)TEM. The aberrations have origin mainly in the shape of the lens magnetic field (described by Maxwell equations), in energy spread of the particles, but also in the imperfect rotation symmetry of lenses or defects in their material [2], [8].

Generally, an image aberration Δw_i can be expressed as a distance between the intersection w_i of a Gaussian (ideal) ray with the image plane (dashed line in *Figure 6*) and the intersection w_i' of the aberrated (real) ray with the image plane (full line in *Figure 6*). Both rays have origin in the object plane and pass through the aperture plane. For HRTEM, the aperture plane is the back focal plane of the objective lens [8].

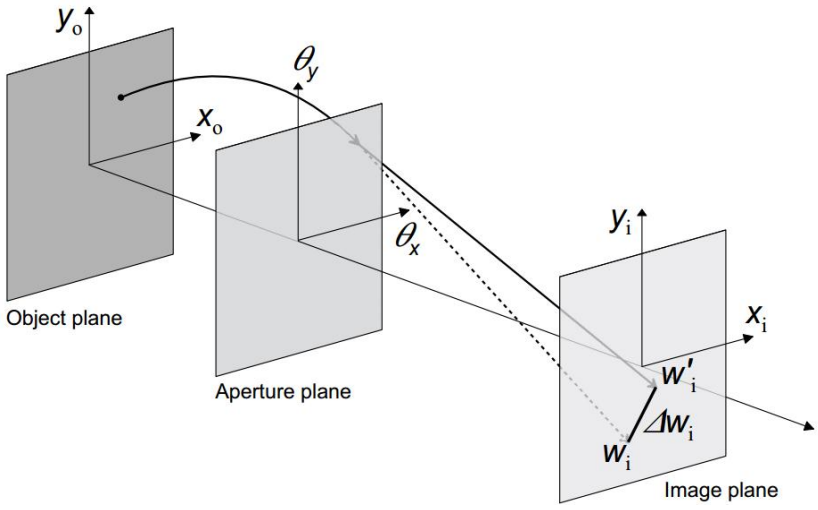

Figure 6: A general image aberration Δw_i [8]

2.1 Chromatic aberration

Let's assume that the **chromatic aberration** primarily cause the loss of information. It is caused namely by the **energy spread ΔE** of the electron beam. The electrons emitted from the electron gun don't have exactly the same energy (wavelength) due to the extracting voltage fluctuations, the instability of the objective lens current, energy loss due to inelastic scattering, etc [2]. The effect is that the electrons of different energies are focused differently by the magnetic lens because of varying focal lengths (*Figure 7*, b) [8].

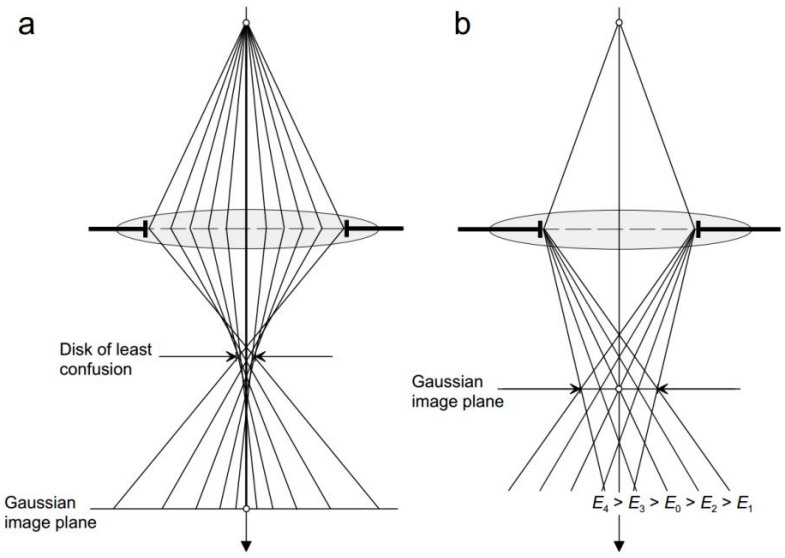

Figure 7: a) Spherial aberration, b) chromatic aberration [8]

2.2 Geometrical aberrations

The geometrical aberrations don't depend on the energy spread of the particles and don't necessarily cause a loss of information, but they mainly affect the interpretability of the TEM images and their geometry due to phase shifts of the electron ray. The geometrical aberrations are namely the spherical aberration, coma, field astigmatism and field curvature and the distortion [8].

2.2.1 Spherical aberration

The magnetic field of a lens is not homogeneous along the whole optical axis. An impact of the spherical aberration is shown in *Figure 7*, a – the rays arriving very close to the optical axis (with small angles) are focused to one point on the Gaussian plane, but the rays coming from larger angles intersect the Gaussian plane in farther from the axis. So a point object is displayed as a disk of finite size on the image. The spherical aberration affects all object points equally and limits the point resolution of the TEM (*Figure 8*) [8].

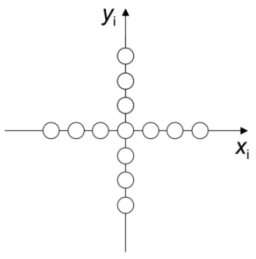

Figure 8: The spherical aberration: each point results in a disk [8]

2.2.2 Coma

The coma aberration causes a point object to be displayed as a specific shape that resembles a comet (*Figure 9*). The effect increases with the off-axial distance. Coma can be minimized by tilting the electron beam [8].

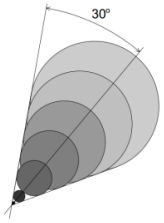

Figure 9: Coma aberration [8]

2.2.3 Field astigmatism and field curvature

The most common **two-fold astigmatism** comes from the fact that the two orthogonal directions of a lens have a different focusing power (which depends on the azimuthal angle). It results from the imperfections in the material or shape of the polepieces. A point object is imaged as a ellipse. This aberration is well correctable by the TEM stigmators [8].

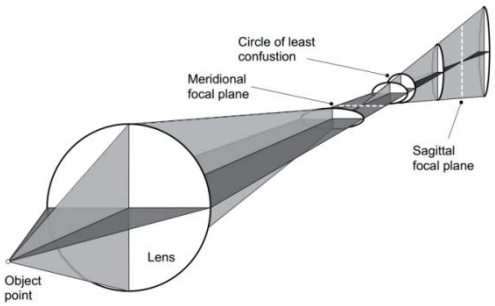

Figure 10: Two-fold astigmatism [8]

The **field curvature** is an aberration causing the defocus varying across the field of view. A point object in a distance *h* from the optical axis is imaged as a disc out of focus. Another point placed in distance *2h* is displayed as four times larger (*Figure 11*). This is the major difference of the spherical aberration impact which influences all points in the same way [8].

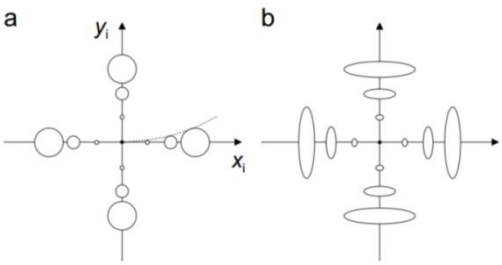

Figure 11: a) Field curvature, b) field curvature combined with field astigmatism [8]

2.2.4 Distortion

The distortion doesn't result in a loss of image information or detail and is purely a geometrical aberration. Each object point has a corresponding object point in the resulting image. The distortion thus doesn't influence the single points, but the total shape of the object. The distortion is most visible in the images of a sample containing straight lines or some periodic structure (atomic lattice) [8].

The most prevalent form of the geometrical distortion is the **barrel** and the **pincushion** distortion. In case of barrel (pincushion) distortion, the magnification of image decreases (increases) with the distance from the optical axis. The helical trajectories of the electrons in the magnetic field can produce also a **spiral or azimuthal** distortion (*Figure 12*). The distortion created by the TEM is commonly a combination of these three types and it is caused mostly by the projector lenses [8].

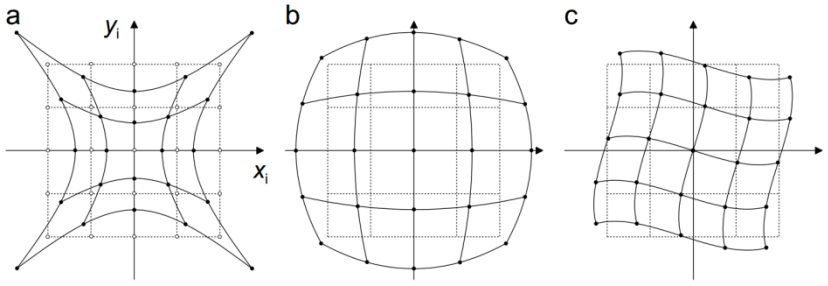

Figure 12: a) pincushion, b) barrel, c) spiral or azimutal distortion [8]

2.3 Aberration coefficients notation

The aberrations are always characterized by the aberration coefficients. A generally accepted notation is ***Krivanek et al. (1999)*** notation which denotes the order (in terms of the wave-vector ***K***) and the azimuthal symmetry of the aberrations. An example is in table *Table 1* and more details in [9].

Table 1: Krivanek notation of some aberration coefficients [9]

Aberration coefficient	Krivanek notation	Order in K	Symmetry
Image shift	$C_{0,1}$	1	1
Two-fold astigmatism	$C_{1,2}$	2	2
Defocus	$C_{1,0}$	2	Inf
Three-fold astigmatism	$C_{2,3}$	3	3
Axial coma	$C_{2,1}$	3	1
Spherical aberration	$C_{3,0}$	4	Inf

3 STATE OF THE ART

This chapter is a brief overview of existing techniques and methods being used in the geometrical distortion correction problem concerning the microscopic crystalline structures. There are mainly two approaches – the techniques working in a **Fourier space** and those in a **real space**.

An exemple of the **Fourier space technique** is a *Geometric Phase Analysis (GPA)* which uses the calculation of phase images through Fourier filtering.

Two exemples of the **real space techniques** (which can be also designated as the *intensity based techniques*) are *Peak finding* (PF) and *Pair Analysis (PPA).* Neverthless, the designation of the "real space" techniques can be misleading here. In in most of cases, this techniques require some pre-processing of the data and it is most commonly a Bragg-filtration of images which is done in Fourier space. So, after all, this methods are in a certain way also Fourier space techniques.

3.1 Geometric Phase Analysis (GPA)

Geometric Phase Analysis (GPA) in concrete realization is a plug-in for *Gatan DigitalMicrograph*, developed by *HREM Research Inc.*, for fully quantitative deformation and strain mapping from high-resolution TEM and SEM (HR(S)TEM) images, or indeed from any type of lattice image. GPA can correct for optical distortions due to the projector lens system of the electron microscope and other elements like CCD cameras and scanners. GPA works with the fact that these geometrical distortions are usually fixed for a given system (microscope). The elimination of these distortions is therefore possible by measuring them only once on a reference image and then correcting subsequent images acquired on the same system.

Theoretically, a Fourier transform of an image of perfect crystal contains strong frequency components (bright spots) called Bragg-reflections (or Bragg spots). These components contain information about the crystalline structure of the input image. Using an asymmetric filter centered at a Bragg spot and applying an inverse Fourier transform gives a complex image whose phase component gives information about the local displacements of atomic planes. The displacement is in the direction of the reciprocal lattice vector stated by

the selected Bragg spot. In case of two-dimensional displacement field evaluation, two non-collinear Bragg spots must be selected and corresponding phase images processed [10].

In the beginning of the GPA procedure, the Fourier transform is applied on the reference image (*Figure 13*, a). In the amplitude spectrum (*Figure 13*, b), two Bragg spots are manually selected (*Figure 13*, b – red circles). Consequently, the phase images corresponding to these spots are created (*Figure 13*, c, d). They are shown in a temperature colour scale (with "phase jumps" from π to -π). On these images, a *reference area* corresponding to the undistorted lattice is selected (it is a smooth area with uniform contrast or gradient – visualized with red square in *Figure 13*, c) [11].

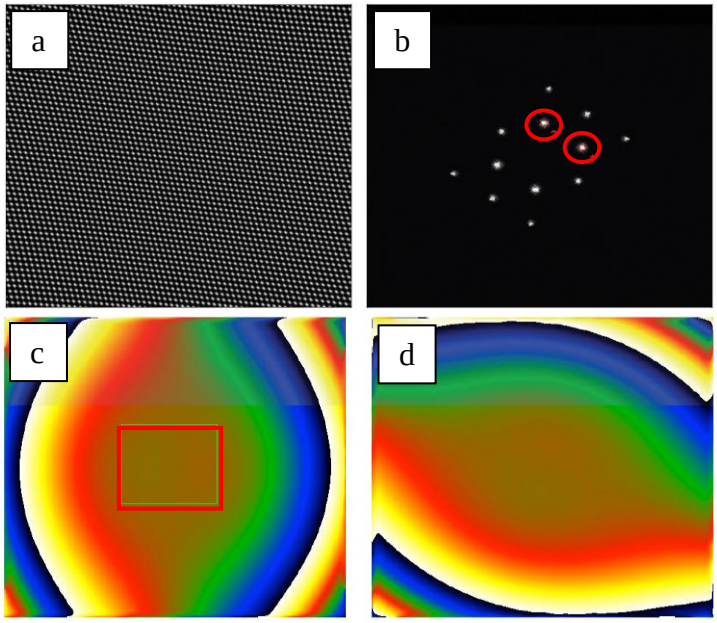

Figure 13: GPA: (a) a reference image, (b) amplitude spektrum, (c, d) phase images [11].

The procedure is then repeated with an experimental image as input. The phase image from the experimental image is divided by the *reference area*. It results into an image containing the difference of phases at *each pixel of the digitized input image.*

When correcting the displacement (distortion), the reference phase is subtracted from the experimental phase in order to obtain the corrected phase image. Those phase images have a nicely uniform appearance. The final result is a corrected image recreated from the corrected phase. GPA also supports a possibility of using a polynomial fit of the selected order (typically of order 3) to the reference phase images before subtracting them from the experimental phases. The result is then much smoother [11].

3.2 Peak Finding method (PF)

Peak Finding method is a real space method for strain analysis of HRTEM images. The procedure involves following steps.

Firstly, the **area of interest** with stable thickness for strain analysis on the input image is chosen (*Figure 14*, a – *InGaAs* sample). The optional step is then **noise reduction** (in this case, different authors propose different solutions, but usually a Wiener filter and a real space averaging is applied).

Next step is **the detection of the lattice sites** in the filtered image. The detection is usually realized by the localization of the maxima of intensity in the input image ("peak-finding"). This is realized by calculation of the mass centers inside chosen circular regions. One of possible solutions suggests the use of a Laplacian operator which points out the centers of the bright dots. Another is fitting a 2D function *z* to the intensity distribution and minimizing the square value of the difference between *z* and intensity function *I*. The desired centre of mass then corresponds to the maximum of *z*.

Subsequently, a **reference area** in the image must be chosen (*Figure 14*, b – *GaAs* sample) and the **base vectors** of the reference lattice are calculated. The reference area should be a bit larger than the area of interest and should be situated out of the deformed region (but this condition is hard to fulfill in practice, so the least deformed zone must be sufficient). There should be optimally around 1000-4000 of atomic columns in this area [12].

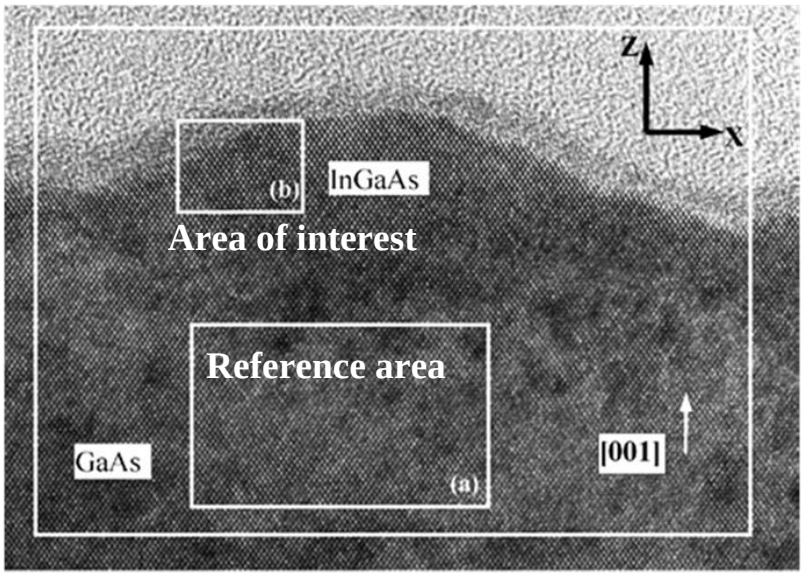

Figure 14: HREM image with the reference area and the area of interest [12]

In this area, a reference lattice (determined by peak finding) can be composed of more sub-lattices. In *Figure 15*, a) there are two sub-lattices and each of them has four parameters (**base vectors**) e_{xx}, e_{xy}, e_{yx} and e_{yy} (*Figure 15*, b) which have been calculated by fitting to the list of the intensity maxima from two starting points x_0 and y_0 [12].

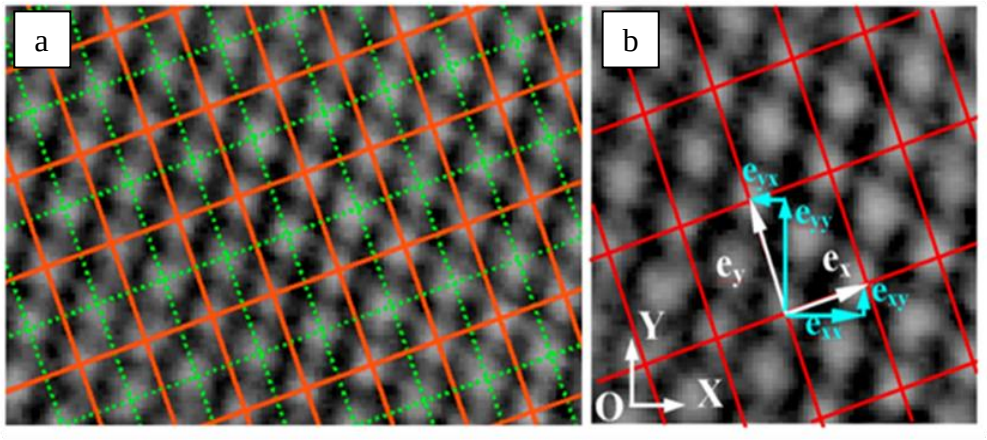

Figure 15: a) Two sub-lattices of the reference area, b) base vectors of one sub-lattice [12]

As a next step, the detected reference lattice is **extrapolated** to the whole image (as well as to the deformed zone of interest. *Figure 16*, a) shows the lattice with nodes in experimental maximum positions (in green) and the extrapolated lattice from the reference area (in red)). Finally, **the displacement** of each experimental lattice site is calculated as a difference between spatial coordinates of nodes of the experimental (distorted) and extrapolated (reference) lattice (shown as red displacement vectors in *Figure 16*, b – the scale is multiplied by 5).

The next steps include averaging to reduce errors, calculation of local lattice parameter by derivation of the displacements, creating maps of the displacement field and other processes [12].

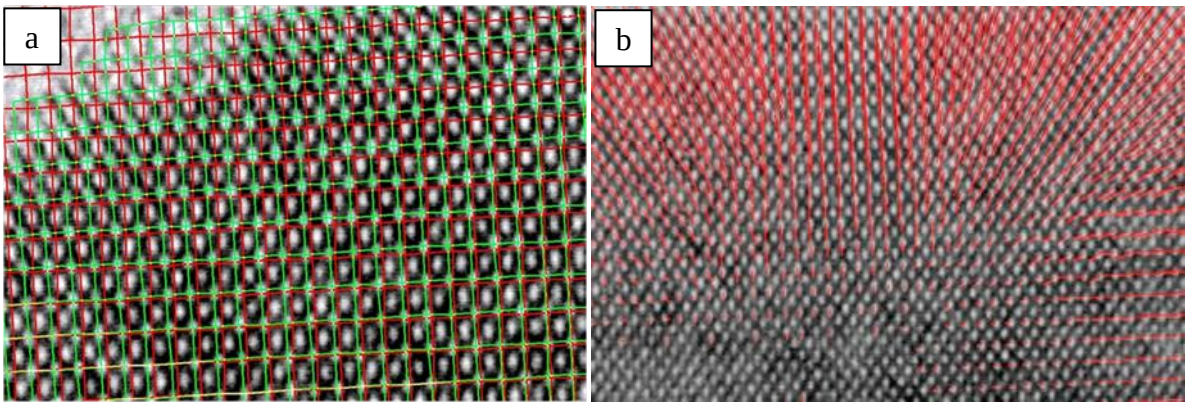

Figure 16: a) The real (green) and extrapolated (red) lattice, b) displacement vectors [12]

3.3 Peak Pairs Analysis (PPA)

Peak Pair Analysis (PPA) is as well as GPA a plug-in for *Gatan DigitalMicrograph*, developed by *HREM Research Inc*. However, the scientific developer of the method is Prof. Pedro L. Galindo who presents this method like a real space procedure for strain mapping on HRTEM images. The method is besides all good for the displacements identifications in the material [13].

The first step of PPA involves, for more efficient intensity maxima determination, a filtration of the input image. The filtration is usually realized by Bragg-filtering or a low-pass or an adaptive Wiener filter. Bragg-filtering is made similarly as in case of GPA, but here more than two spots in a power spectrum are selected (for preservation of most of the intensity maxima), the mask is placed around these spots and the inverse Fourier transform is applied [14].

After the filtration, all the (local) intensity peaks are detected using 8-connected neighbourhood maxima comparisons in each pixel. If all neighbourhood's intensity values are smaller than the intensity of the central pixel, this pixel is designated as a local maximum. For a sub-pixel resolution, there are two possible approaches – 2D interpolation and function maximization through fitting a 2D quadratic function around each local maximum (more details in [14]).

PPA involves, like in case of PF, the necessity of presence of a reference (non-distorted) area far away from the defects (distorted areas) to be analyzed. In this (reference) area, three points (A, B, C) corresponding to the maximum intensity are selected and thus, two non-collinear basis vectors $\vec{a}, \vec{b}$ are determined (*Figure 17*) [14].

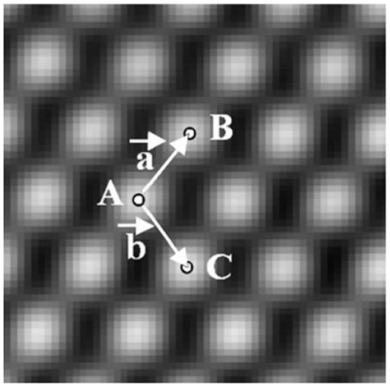

Figure 17: Points A, B, C and two basis vectors $\vec{a}, \vec{b}$ in the reference area [14]

The basis vectors allow to evaluate the intensity maxima in positions given by the equation $A + m \cdot \vec{a} + n \cdot \vec{b}$, where *m* and *n* denote integers.

The corresponding coordinates of the determined intensity maxima are then transformed by an affine transformation which preserves the parallelism of lines. The transformation is given by a transformation matrix containing six unknown parameters, which can be defined thanks to three control points A, B and C (or point A, and vectors $\vec{a}$ and $\vec{b}$ respectively). A is transformed into (0,0), the vector components (a_x, a_y) into (1, 0) and (b_x, b_y) into (0,1). If this transformation is applied on a non-distorted material, it would produce a perfectly square grid. But the experimental image produces only a near-square grid where the deviations are easy to identify. *Figure 18* illustrates the situation - *Figure 18*, a) shows the Bragg-filtered image of *CdTe* material containing dislocations with basis vectors $\vec{a}, \vec{b}$ (scale multiplied by 5) and the *Figure 18*, b) visualizes an affine-transformed image with the dislocations [14].

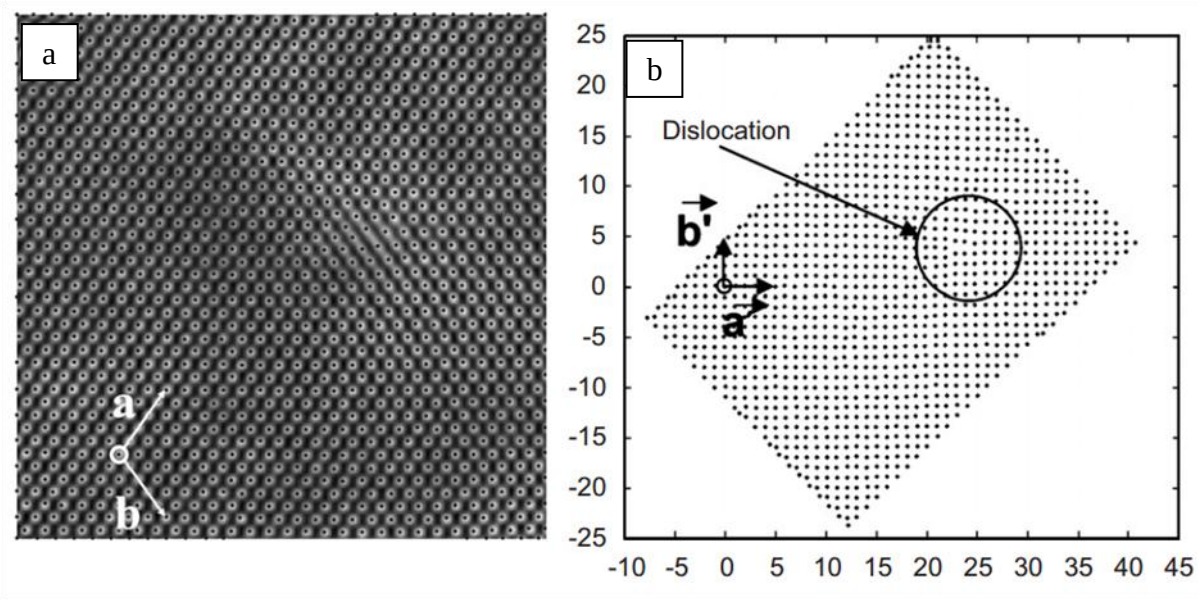

Figure 18: a) A Bragg-filtered image of CdTe b) an affine-transformed image [14]

Consequently, the P*airs of Peaks* can be determined. Each intensity maximum *(x, y)* has an associated "partner" in the direction of $\vec{a}$ and $\vec{b}$ and in the distances $|\vec{a}|$ and $|\vec{b}|$ respectively. The identification of these peaks is performed in the transformed image (because it greatly reduces potential errors) considering the smallest Euclidean distances between peak-coordinates. The detected pairs of neighbours are then connected by single lines, which enables to visualize various dislocations in the material (*Figure 19*, a).

The final displacement field $u=(u_x, u_y)$ and $v=(v_x, v_y)$ of peaks in coordinates (x_1, y_1) and (x_2, y_2) that are both neighbours of peak in (x_0, y_0) can be calculated using the basis vectors $\vec{a}$ and $\vec{b}$ as follows:

$$\begin{aligned} u_x &= x_1 - x_0 - a_x\,, & v_x &= x_2 - x_0 - b_x\,, \\ u_y &= y_1 - y_0 - a_y\,, & v_y &= y_2 - y_0 - b_y\,, \end{aligned} \tag{7}$$

where the variables denote coordinates and vector components that are graphically visualized in (*Figure 19*, b). The peak is present in (x_0, y_0) and its two neighbours in (x_1, y_1) and (x_2, y_2) coordinates [14].

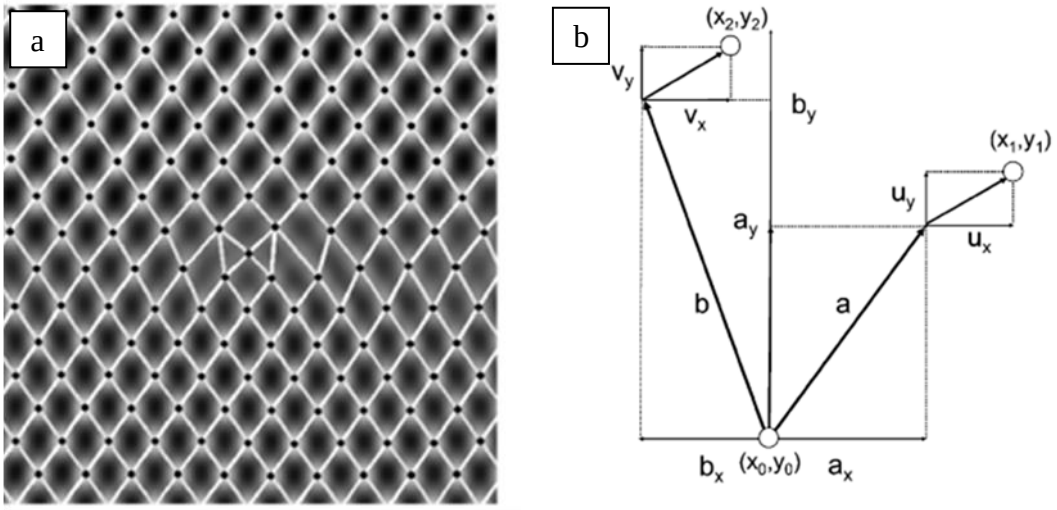

Figure 19: a) Visualisation of dislocations, b) calculation of the displacement field [14]

After calculating the lattice distortion for each maximum in the image, the continuous distortion is determined by simple 2D interpolation [14].

The PPA tool for the Digital Micrograph enables to show the displacement maps as well as correcting the distortions. When considering only the defects caused by the microscope lenses and CCD cameras and not the dislocations in the material, the correction of distortion of an image can be quickly done after the displacement measurement on a calibration image of a perfect crystal. The process is similar to the GPA method [13].

4 IMAGE REGISTRATION

The aim of image registration process is to find an appropriate ***geometrical transformation T(x)*** whose application to one image results in the best possible overlapping of the pair of images. The two images are designated as the ***fixed (reference) image $I_F(x)$*** (the original image from the imaging device) and the ***moving image $I_M(x)$*** (the model of scene) to be geometrically transformed for the best superimposition with $I_F(x)$ *[15]*.

The registration methods can be divided into several groups. One of these groups is according to modality of image acquisition. The registration can be considered **intramodal** or **multimodal**. **Intramodal** image registration works with data acquired by the same device. **Multimodal** image registration aligns data acquired by different devices or the image with its model (model-based image registration). Another groups concern images acquired in different time or viewpoint [16].

According to the nature of the data, the image registration is **interactive** or **unaided**. In case of the **interactive** image registration, the process is guided by a human operator who may aid by manual selection of reference points in both images. This approach requires the presence of typical (unique) points which can be clearly detectable in the image (not the case of image of atomic lattice). In a contrary, the **unaided** (unassisted) image registration generates the solution without the human intervention and typically involves the application of an **optimization algorithm** that optimizes a **criterion function** [17], [18].

Respecting the task of this work and the nature of the data, let´s focus on the **multimodal** (image from TEM and a model artificial grid) and **unaided** image registration.

The general scheme of registration process is in *Figure 20* and described below.

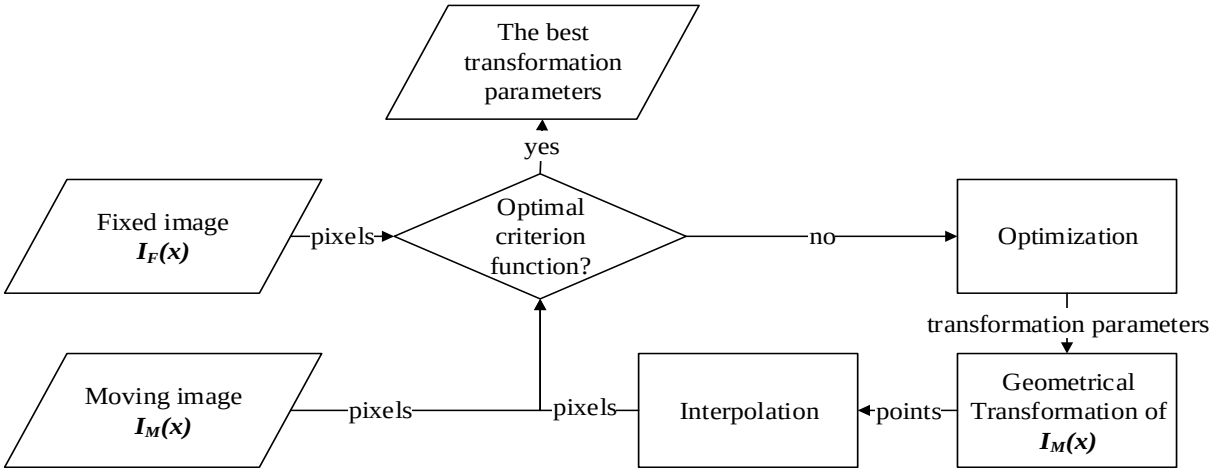

Figure 20: The image registration process [19]

As shown in *Figure 20*, the image registration is an iterative process. Firstly, the input images $I_F(x)$ and $I_M(x)$ are compared in terms of their similarity by computing a value of a criterion function (similarity criterion – 0). Secondly, depending on a terminating condition or a number of iterations, the optimization algorithm (4.3) does the estimation of the new transformation parameters and consequently, the geometrical transformation (4.1) is applied on the moving image $\boldsymbol{I_M(x)}$. The transformation of coordinates is followed by an interpolation and creation of a deformed (transformed) image $\boldsymbol{I'_M(x)}$. $\boldsymbol{I'_M(x)}$ should be ideally more similar to the fixed image $\boldsymbol{I_F(x)}$ than in the previous iteration. Subsequently, the criterion function is calculated again and the iterative optimization process continues till the best possible registration of the images is reached. The output is then the transformation parameters leading to the best similarity overlap.

Following chapters 4.1, 4.2 and 4.3 introduce the preliminary theory for the image registration.

4.1 Geometrical transformations

Geometrical transformation in general consists of two steps:

- First, **the transformation of points coordinates** and
- second, **the approximation of an intensity function (the interpolation)**.

4.1.1 The transformation of coordinates

The transformation of descrete coordinates involves the recalculation of the input (x,y)-coordinates to the output (x',y')-coordinates. The transformation is mainly effected by the image operations such as rotation, scale change, shift etc.

Vector $\vec{r}$ denotes a position vector of x and y coordinates, and $\overrightarrow{r'}$ denotes its tranformation vector. Image I'_M denotes the transformed image I_M by transformation T, as follows [20]:

$$\vec{r} = (x, y) \tag{8}$$

$$\overrightarrow{r'} = (x', y') = T(\vec{r}) \tag{9}$$

$$I'_M = T(I_M) \tag{10}$$

General transformation matrix

The general transformation coefficients can be expressed in 3×3 matrix [21]:

$$\begin{bmatrix} a_{11} & a_{12} & a_{13} \\ a_{21} & a_{22} & a_{23} \\ a_{31} & a_{32} & a_{33} \end{bmatrix} \tag{11}$$

Affine transformation

The affine transformation is a most general linear transformation that preserves collinearity and ratios of distances. The affine transformation parameters can be also expressed in form of 3×3 matrix that is characterized by the last column equal to $[0 \quad 0 \quad 1]^T$, as follows [21]:

$$T_{affine} = \begin{bmatrix} a_{11} & a_{12} & 0 \\ a_{21} & a_{22} & 0 \\ a_{31} & a_{32} & 1 \end{bmatrix} \tag{12}$$

The output *x'* and *y'* is then calculated as follows:

$$[x' \quad y' \quad 1] = [x \quad y \quad 1] \cdot \begin{bmatrix} a_{11} & a_{12} & 0 \\ a_{21} & a_{22} & 0 \\ a_{31} & a_{32} & 1 \end{bmatrix} \tag{13}$$

$$x' = a_{11}x + a_{21}y + a_{31} \tag{14}$$

$$y' = a_{12}x + a_{22}y + a_{32} \tag{15}$$

According to the two previous equations, the affine transformation is also a polynomial transformation of first order. The coefficients a_{31} and a_{32} mainly affect the translations, a_{11} and a_{22} affect the scale changes and a_{21} with a_{12} affect both the rotations and shears [22].

As mentioned, the elementary transformations like *translation*, *rotation*, *scale* and *shear* can be combined and lead to the composite affine transformation. Following equations show the possible combination of the three mentioned transformations (without shear) [21]:

$$T_{composite} = T_{translation} \cdot T_{rotation} \cdot T_{scale} \tag{16}$$

$$T_{composite} = \begin{bmatrix} 1 & 0 & 0 \\ 0 & 1 & 0 \\ T_x & T_y & 1 \end{bmatrix} \cdot \begin{bmatrix} cos\,\Theta & sin\,\Theta & 0 \\ -sin\,\Theta & cos\,\Theta & 0 \\ 0 & 0 & 1 \end{bmatrix} \cdot \begin{bmatrix} S_x & 0 & 0 \\ 0 & S_y & 0 \\ 0 & 0 & 1 \end{bmatrix} \tag{17}$$

$$T_{composite} = \begin{bmatrix} S_x\,cos\,\Theta & S_y\,sin\,\Theta & 0 \\ -S_x\,sin\,\Theta & S_y\,cos\,\Theta & 0 \\ S_x\,(T_x\,cos\,\Theta - T_y sin\,\Theta) & S_y\,(T_x\,sin\,\Theta + T_y cos\,\Theta) & 1 \end{bmatrix} \tag{18}$$

Projective transformations

The matrices of the projective transformation coefficients have the last column $[a_{13} \quad a_{23} \quad 1]^T$ nonzero. These transformations are associated with the tilt of the image plane relative to the object plane and with the change of perspective [21], [22].

Polynomial transformations

Polynomial transformations are often used for the correction of an unknown distortion function and are mainly utilized in medical imaging and computer vision. They are associated with spatial distortions such as *centering, scale, skew, barrel* and *pincushion* effects, *field of vue change, lens defects, altitude effects, terrain relief*, etc (*Figure 21*) [21].

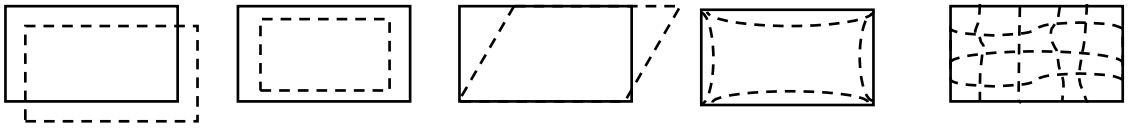

Figure 21: Some examples of the distotion [21]

The transformation of the coordinates can be represented by the polynomial of m[th] order, as follows:

$$x' = \sum_{r=0}^{m} \sum_{k=0}^{m-r} a_{rk} x^r y^k \tag{19}$$

$$y' = \sum_{r=0}^{m} \sum_{k=0}^{m-r} b_{rk} x^r y^k \tag{20}$$

where a_{rk} and b_{rk} are the constant coefficients an m is a degree of the polynomial [21].
For the first order polynomial (m = 1):

$$\begin{aligned} x' &= a_0 + a_1 x + a_2 y \\ y' &= b_0 + b_1 x + b_2 y \end{aligned} \tag{21}$$

For the second order polynomial (m = 2):

$$\begin{aligned} x' &= a_0 + a_1 x + a_2 y + a_3 xy + a_4 x^2 + a_5 y^2 \\ y' &= b_0 + b_1 x + b_2 y + b_3 xy + b_4 x^2 + b_5 y^2 \end{aligned} \tag{22}$$

For the third order polynomial (m = 3):

$$\begin{aligned} x' &= a_0 + a_1 x + a_2 y + a_3 xy + a_4 x^2 + a_5 y^2 + a_6 x^2 y + a_7 xy^2 + a_8 x^3 + a_9 y^3 \\ y' &= b_0 + b_1 x + b_2 y + b_3 xy + b_4 x^2 + b_5 y^2 + b_6 x^2 y + b_7 xy^2 + b_8 x^3 + b_9 y^3 \end{aligned} \tag{23}$$

4.1.2 The interpolation

The newly calculated coordinates from the previous step are usually continuous and doesn't match to the output digitized image. So the appropriate intensity value in the new position should be evaluated. The approximation of an intensity function searches for a value in the integer position best corresponding to the newly computed non-integer position (x',y'). It is usually done using the **interpolation methods**.

The most commonly used interpolation methods of two-dimensional (2D) data are the **nearest neighbour**, the **bilinear interpolation** and the **bicubic interpolation**. There is always a need to specify the requirements to the resulting image quality and computation speed before choosing the interpolation method [18].

Nearest neighbour

Nearest neighbour is the simplest and fastest interpolation method. It consists in choosing the nearest pixel to the calculated non-integer position and assuming its intensity value. The choice of the nearest pixel is mathematically executed by rounding both coordinate values. The method is quick, but it causes a loss of apparent resolution (visible sharp edges) [18]. The principle is shown in *Figure 22* - in this case, *p(x',y')=p(x,y+1).*

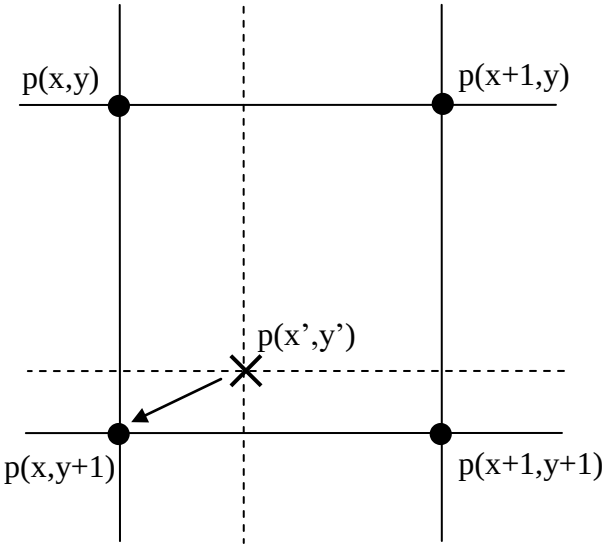

Figure 22: The nearest neighbour interpolation [23]

Bilinear interpolation

Bilinear interpolation computes the desirable value as a weighted average of four nearest pixels. According to *Figure 23*, the *p(x´,y´)* value is computed as a sum of individual point values multiplied by the opposite rectangle (of the same colour) divided by the total area of all four rectangles. In this case, the violet point *p(x,y+1)* has the biggest weight, so it´s intensity value will create the biggest fraction of the result (and this point is actually the nearest to *p(x´,y´))* [18]. The weights are the relative areas of the **opposite** rectangle in the image below. The result is smoother than in case of the nearest neighbour.

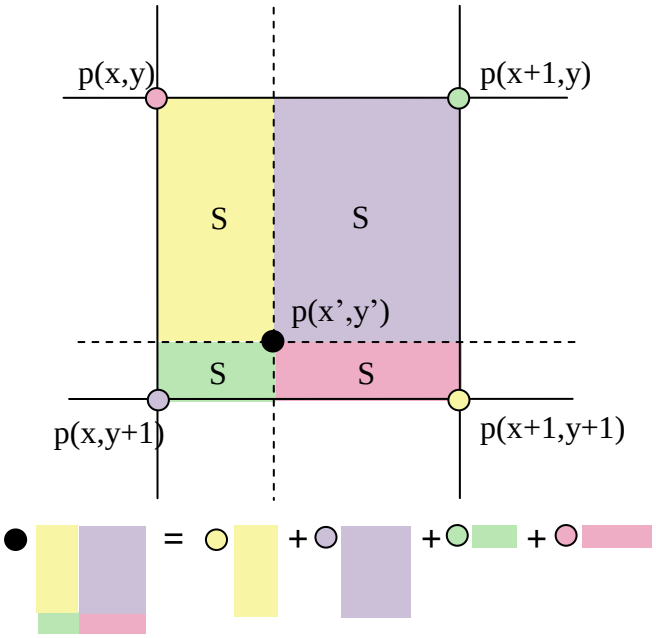

Figure 23: Bilinear interpolation [24]

Bicubic interpolation

Bicubic interpolation computes the desirable value using sixteen surrounding pixels using either the cubic splines, Lagrange polynomials or cubic convolution algorithm. This method brings the smoothest result of the mentioned methods but the computational demands are much bigger [18]. The differences between all three methods are shown in *Figure 24*.

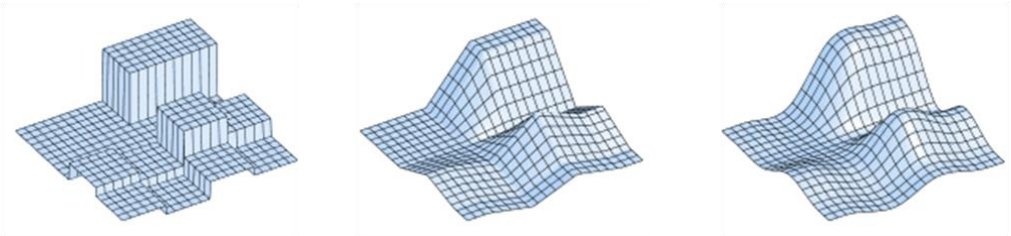

Figure 24: Nearest neighbour (left), bilinear (middle), bicubic interpolation (right) [25].

4.2 Criterion functions

An important step in image registration is a choice of a criterion function to be optimized. The choice of the criterion depends on a nature of the data to be registered. The optimization generally involves minimization or maximization of the criterion function (but the minimization tasks can be converted into maximization tasks and vice versa). The global similarity criteria (criterion functions) can be divided into two groups: **intensity-based** or **information-based** criteria.

4.2.1 Intensity-based criteria

The intensity-based similarity criteria are suitable mainly for the intramodal data (data acquired by the same device).

Sum of Squared Differences (SSD)

SSD is the simplest method for comparing the fixed $\boldsymbol{I_F(x)}$ and the transformed moving $\boldsymbol{I_M'(x)}$ image. The images are subtracted, the differences for all pixels $\boldsymbol{N}$ are squared and averaged. The result is one value. The optimal solution is the minimal value of SSD (zero in case of identical images). The SSD can be calculated as follows (***i*** represents the pixel count) [20]:

$$SSD = \frac{1}{N}\sum_{i}^{N}|I_F(i) - I'_M(i)|^2 \tag{24}$$

Correlation Coefficient (CC)

The correlation coefficient of $\boldsymbol{I_F(x)}$ and $\boldsymbol{I_M'(x)}$ is calculated like multiplication and sum of all pixels. The method is fast but not very robust. The optimal solution is the maximum value of CC. The CC can be calculated as follows [20]:

$$CC = \sum_{i} I_F(i) \cdot I'_M(i) \tag{25}$$

Cosine similarity (Cos)

Cos is a similarity measure computing the angle between the vectors $\vec{a}$ and $\vec{b}$, where $\vec{a}$ is the vector of intensities from I_F and $\vec{b}$ is the vector of intensities from I'_M. The result is normalized into the <0,1> range [20]:

$$Cos(\vec{a},\vec{b}) = \frac{\sum_i \vec{a}_i \vec{b}_i}{\sqrt{\sum_i \vec{a}_i^{\,2} \cdot \sum_i \vec{b}_i^{\,2}}} \tag{26}$$

4.2.2 Information-based criteria

The information-based similarity criteria are, one the other hand, suitable mainly for the multimodal data (data acquired by different device), because the contrast in the image can differ significantly [20], [26], [27].

Joint histogram

To compare the intensities of two images (A and B) to be registered, a two-dimensional joint histogram can be used. It is a matrix with dimensions [*q*,*r*], where *q* is a number of gray shades in image A and *r* is a number of gray shades in image B (*Figure 25*). If these two images are identical, the joint histogram would be a diagonal line [20].

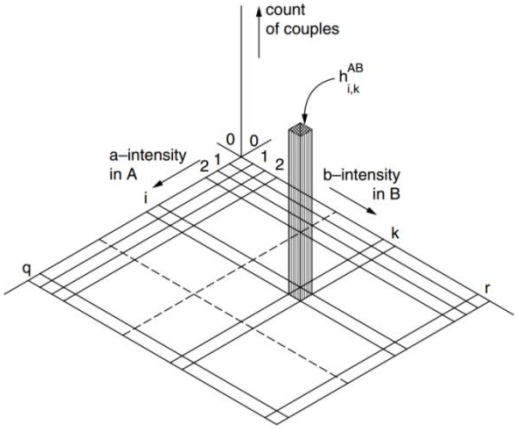

Figure 25: Scheme of the two-dimensional joint histogram with one intensity value [20]

Mutual Information

The marginal probabilities p_A and p_B and the probability of occurrence of a pair of values p_{AB} in the concrete coordinates in both images are defined as follows [20]:

$$p_A\{l\} \approx \frac{1}{N} h_l^A \tag{27}$$

$$p_B\{m\} \approx \frac{1}{N} h_m^B \tag{28}$$

$$p_{AB}\{l,m\} \approx \frac{1}{N} h_{l,m}^{AB}, \tag{29}$$

where h_l^A, h_m^B and $h_{l,m}^{AB}$ are the vectors with the length corresponding to the number of gray scales, where each value denotes the total number of this gray level in the image, *N* is a total number of pixels in the image, *l* and *m* are intensity values in images. The $h_{l,m}^{AB}$ is calculated from the joint histogram.

The individual entropies H_A and H_B and the joint entropy H_{AB} are defined as follows [20]:

$$H_A = -\sum_{l=1}^{q} (p_A\{l\}) \cdot log\ (p_A\{l\}) \tag{30}$$

$$H_B = -\sum_{m=1}^{r} (p_B\{m\}) \cdot log\ (p_B\{m\}) \tag{31}$$

$$H_{AB} = -\sum_{l=1}^{q}\sum_{m=1}^{r} (p_{AB}\{l,m\}) \cdot log\ (p_{AB}\{l,m\}) \tag{32}$$

These entropies are proportional to the information in images A, B and the image union AB, respectively. The mutual information I_{AB} can therefore be calculated as:

$$I_{AB} = H_A + H_B - H_{AB} \tag{33}$$

The mutual information expresses the similarity between the two images. In case of two identical images, the I_{AB} would be maximum. The goal during the registration is to find a maximum value of the mutual information considering to be a criterion function [20].

4.3 Optimization algorithms

The optimization algorithms are searching for the optimal solution of a given problem in the most effective way. As mentioned, all optimization problems searching for the maximum of the criterion function can be converted into searching the minimum by simple sign change. Let´s assume then, that an optimization algorithm is searching for a geometrical transformation T_{opt} with the parameters enabling to minimize the global similarity function *F* of the fixed image $I_F(x)$ and the moving image $I_M(x)$ transformed by the geometrical transformation *T* [28].

$$T_{opt} = arg\ min_T\ F(T(I_M), I_F) \tag{34}$$

The **deterministic** optimization methods often work with the first and second derivations of the analyzed function and require the knowledge of the previous state. These

methods in many cases find only a local optimum of the given problem. The deterministic algorithm are for example *gradient methods* (*Gradient descent* and *Newton's method)*, *Exhaustive search* and the *comparative methods (Box-Wilson* and *Simplex method)* [28], [29], [30].

The **stochastic** optimization methods can usually overcome this problem and find the global optimum. The stochastic algorithms use heuristics to find a new state. They use the random processes, intuition and experience. The stochastic algorithms are for exemple *Random search, Controlled random search (CRS)* and *Simulated annealing* [28], [31], [32], [33], [34], [35].

A combination of the deterministic and stochastic algorithms are the *metaheuristic* algorithms also called as evolutionary or **genetic algorithms** [28], [31]. Following chapters present some selected methods.

4.3.1 Gradient descent and Newton's method

As the name tells, **gradient descent** searches for an optimum using a gradient of the criterion function in a point (or in a small neighborhood). In every iteration, the first derivation of the function is evaluated. The point in the direction of the biggest gradient becomes the next state. The method can converge to the global or local optimum depending on the initial estimated position (initial parameters). Also, depending on the sampling step, the global optimum can be skipped [29].

Newton's method is also a gradient method. This method approximates the neighborhood of a point by a parabola and a new state is a minimum (or maximum) of this function. The method requires the estimation of a Hessian matrix (and first and second derivation in every iteration) which is quite computationally demanding. Newton's method can be realized in Matlab using *fminunc* function [28], [30].

4.3.2 Exhaustive and random search

Exhaustive search browses through all the possible combinations of the searched transformation coefficients. The solution is chosen as the best solution in terms of the optimal criterion function. This method should find the optimal solution always, but the limitation is in used sampling step. Because of high computation demands, the solution can be first estimated with rough sampling and then refined with fine sampling [28].

Random search works similarly, but the combinations of the transformation parameters are set randomly in every iteration and the best solution is constantly memorized. The process ends after the set number of iterations. A convergence to the optimum is not guarantee for a small number of iterations [28].

4.3.3 Box-Wilson and Simplex method

The *Box-Wilson* and the *Simplex method* are the *comparative methods*. They compare the functional values in few points. After every iteration, the best value becomes the new approximation of the solution for next iteration.

The **Box-Wilson method** uses the comparison of the functional values at (2^N+1) points, where N is the number of the function dimension. In the simplest form it is a 2D function and 5 points forming a square and its centre. The algorithm ends if the centre of the square is indicated as the best approximation [28].

The **Simplex method** uses a simplex, what is generally a shape formed by N+1 vertices in the N-dimensional space. In 2D space, it is a triangle. In every iteration, the vertices of the triangle are indicated as the best (B), good (G) and the worst (W). The W point is replaced by a point with better quality. It can be done using operations such as reflection (R), extension (E), contraction (C) or shrinking (S) – visualised in *Figure 26*. The basic form of the Simplex method is called *Nelder-Mead algorithm* which can be realized in Matlab by *fminsearch* function [28].

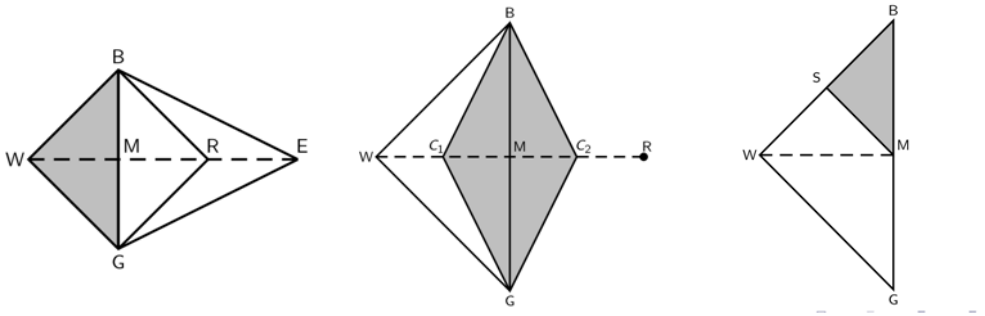

Figure 26: The point operations in the Simplex method [28]

4.3.4 Controlled random search (CRS)

Controlled random search is a simple and effective algorithm searching for a global optimum. CRS works with a population of *N* points in the *d*-dimensional space (each point is a vector of parameters of the searched geometrical transformation). Generally, *N* should be

much bigger than the dimension *d* (for example N=40 in d=2). A heuristic method used for generating a new point *y* is the **reflection** of simplex, known from the *Simplex method*. A simplex is formed by randomly chosen (d+1) points from the population *N*. Consequently, the new point *y* is compared to the worst point W from the whole population and if it is better, than *y* replaces W. The reflection of simplex is expressed as follows [31]:

$$y = 2g - x, \tag{35}$$

where *y* is the new point, g is the center of gravity of the remaining points of simplex and *x* is the point of simplex with the maximum (worst) quality.

The population gradually concentrates among the searched extreme.

There exist many possibilities how to generate new points besides the reflection. One of them is using the previously mentioned procedure with the simplex containing always the best point from the actual population. Another possibility is to use a randomized reflection. The new point *y* is generated as [31]:

$$y = g + U(g - x), \tag{36}$$

where *U* is a random variable from a suitable distribution. Ideally, U is from the uniform distribution with limits [0,α), where α is an input constant determining the convergence speed, e.g. α=4. The used heuristic function can be also based on the genetic algorithms.

The end of CRS algorithm is determined by the end condition. It can be for example a defined number of iterations. Another possibility is to end the algorithm in the moment, when the difference between the functional values of the best and the worst point is smaller than the input parameter ε [31], [32], [34].

4.3.5 Simulated annealing

Simulated annealing is a method inspired by the metallurgic annealing. It's a process when a heated body (metal) is slowly cooled down and the internal defects in the crystalline lattice of the body are reduced.

Like a stochastic optimization method, simulated annealing can be used to find a global optimum of the criterion function. In each step of optimization, a new better solution is generated but also a worse solution can be accepted with a certain probability (which can lead to escaping from the point of local optimum). This probability of accepting the worse solution

is proportional to the temperature. Initially the temperature is very high and the probability of leaving the current state is relatively big. The probability p of accepting the new state is given by the *Metropolis criterion*, expressed as follows:

$$p(\Delta f, T) = e^{\left(-\frac{\Delta f}{T}\right)}, \tag{37}$$

where $\Delta \boldsymbol{f}$ is the difference between the functional values of the current and new state and T is the temperature.

Simulated annealing used for the image registration takes the states as vectors of coefficients of the searched geometrical transformation and the function to be optimized is the criterion of non-similarity [33], [34], [35].

4.3.6 Genetic algorithms

The genetic algorithms are based on the Charles Darwin's evolutionary theory. The algorithms operate with the population of individuals (of potential solutions of the searched coefficients). The coding can be binary or natural (continuous). In case of more dimensions of the examined space (more transformation coefficients), the values are arranged consecutively in the columns of a matrix. The rows represent the individuals. The individuals are progressively (in cycles) modified (improved) by application of the principles of survival. Every individual has its adaptation ratio called *fittnes* or *quality*, which is usually its functional value. The fitness is understood as a rate of survival and the probability to transfer genes to offspring. The individuals of each generation undergo processes as *selection*, *crossover* and *mutation* [31].

The *selection* can have more versions. Usually a higher fitness value means a higher probability to be selected to the next generation. A *roulette wheel selection represents* one of the selection type. Each individual imaginarily occupies a section of a roulette wheel proportional to it's fitness. To choose new individuals for the next generation, random numbers are generated and according to it's belonging to the section of wheel (through calculating the distribution function of probability), the respective individuals are chosen to „survive". A *battle* selection means that in every iteration a set of battles according to number of individuals is executed and every time the one (from a random pair) with better fitness survives.

The *crossover* is done to combine traits from the selected chromosomes and passing them to the next generation. According to the probability of crossover, two individuals are combined by changing a part of their „body“ (it means a part of the binary number).

The *mutation* is a process when a random allele mutates (in binary coding the value alters from 1 to 0 and vice versa) with a certain probability of mutation. This process enables to escape from the local optimum.

Also, an *elitism* can be used, which means that always the best individual passes to the next generation.

The functional blocs of the genetic algorithm can be different according to the specific problem and purpose. The procedure ends for example after a determined number of iterations or after a set of iterations with no considerable improvement [28], [34].

5 PROPOSED REGISTRATION METHOD

5.1 An outline of the method

Image registration is a good instrument how to geometrically align two images. It may therefore be a good way how to correct a image distortion. Illustratively, a sample of a perfectly regular crystal (gold) has a completely squared atomic lattice but the imaging system of TEM enters to the image some distortion (*Figure 27*).

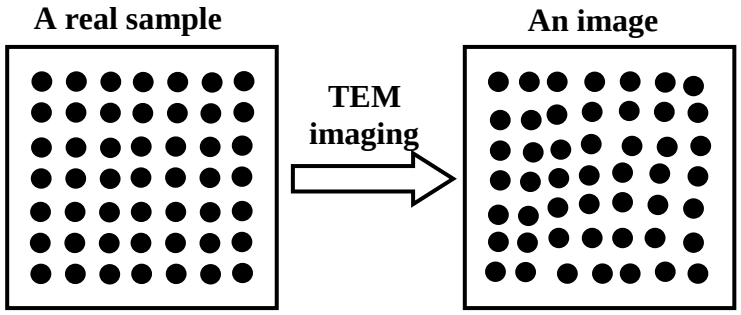

Figure 27: Left: A regular crystal, Right: The image acquired by TEM

Registering the distorted image (moving image) to a regular artificial model grid (fixed image) (*Figure 28*) should lead to realigning of the image.

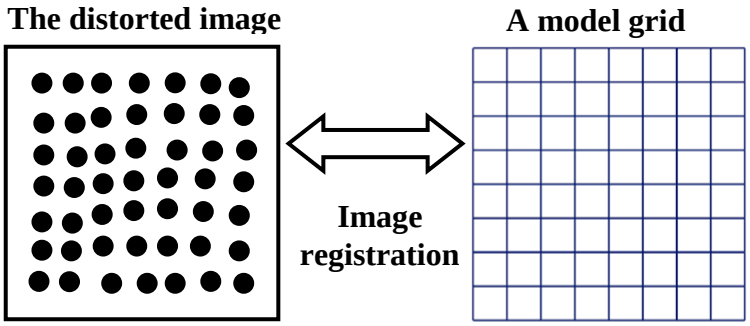

Figure 28: Two images to be registered

The registered moving image then becomes the best possible approximation of the real sample (*Figure 29*).

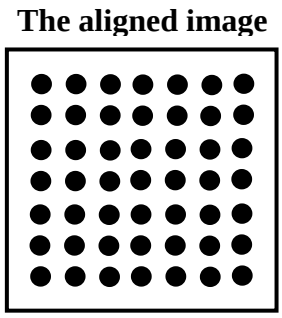

Figure 29: The desirable result after the registration

5.2 Registration algorithm

The image registration is a complex task with many contributors such as transformation function, criterion function, optimization method etc. A method in this work was designed with respect to the data to be processed. *Figure 30* represents a proposed registration algorithm in summary. The individual steps of the registration are discussed in more detail in following chapters.

The steps of registration are:

- Initiation of images (loading the *moving image* and creating the *fixed image*),
- Setting of the registration parameters (image / population size, iterations etc.),
- Creation of an entry generation by **Random population search**,
- Optimization using **Controlled random search** with **Simulated annealing**,
- Improvement of the result by **Gradient descent** and
- Application of the resulting set of parameters (=the best individual with the best quality) to geometrically transform (=correct) the input image.

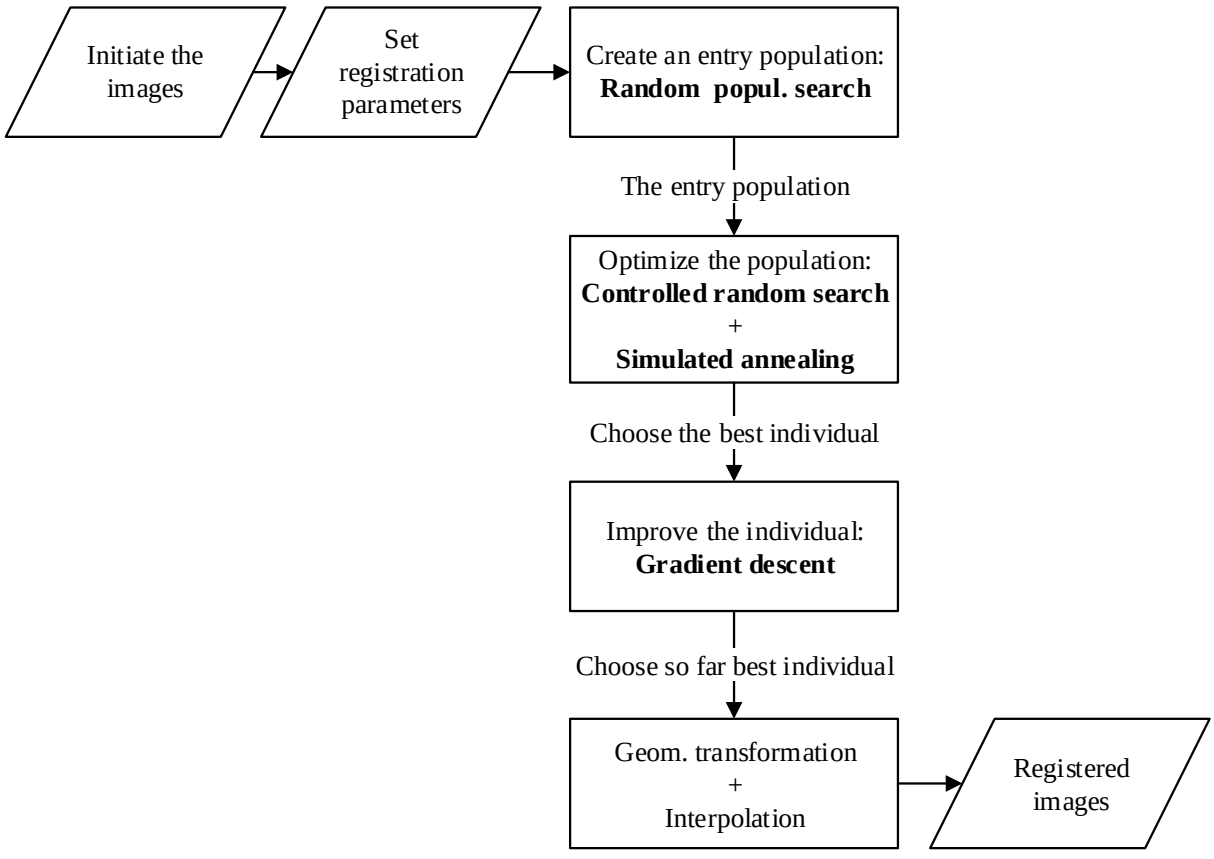

Figure 30: Proposed registration algorithm

5.3 Initiation of images

5.3.1 Moving image

The (moving) image to be corrected is an image of a mono-crystal of gold (Au) with 0.204 nm spacings between the atomic columns displayed in TEM bright field (*Figure 31*). The image is formed especially by the mass contrast (Z). The individual atoms are represented as white dots on a dark background. The distortion is not much visible by eye, but it is present mainly in the corners of the image. The distortion manifests in image as unequal distances between the atomic lines. It was observed that the difference between two atoms in the center of the image and two atoms in the corner may differ even by 1/10 of their distance.

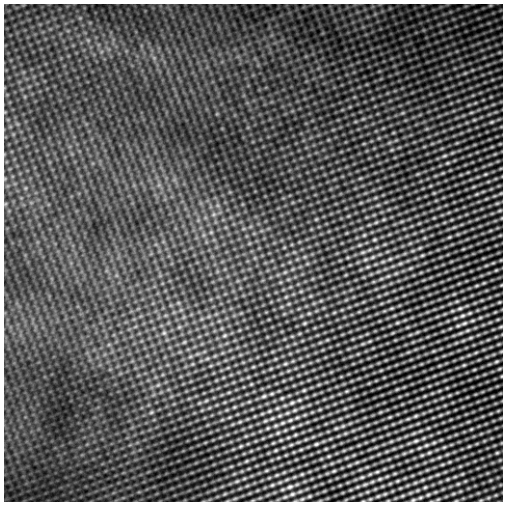

Figure 31: Au monocrystal, TEM bright field

5.3.2 Fixed image

A fixed image is created in Matlab in order to best simulate the atomic lines. First it is necessary to determine a tilt of the atomic lines and rotate the model grid in the same way. It can be done using a Fourier Transform (FT) of the image. Matlab returns the 2D discrete Fourier Transform of the input image with help of *fft2* command. The DFT created in Matlab is a matrix with amplitude and phase component. They can be separated using the *abs(DFT)* and *angle(DFT)* commands respectively. The matrices are of the same size as the input image. Concerning the amplitude component (amplitude spectrum), the low frequencies are present in the corners and the high frequencies in the center. But the spectrum is usually displayed with low frequencies (0,0) in the centre. It can be rearranged using the *fftshift* comand in Matlab [20]. Example of the amplitude spectrum with (0,0) frequency conmponent in the center is in *Figure 32*, left.

The amplitude spectrum gives information about the spectral components in the image. The bright spots (Bragg spots) in the spectrum give information about the most represented angles in the original image. The 2D DFT has a conjugate symmetry, so the two quadrants carry the complete spectral information [20]. In the spectrum of the image of atomic lattice, the most visible should be the components giving the information about the tilt of atomic lines. Considering the two first quadrants of the spectrum, there should be two dominant spots (represented as red dots in *Figure 32*, left) giving information about the two dominant angles (atomic rows and atomic columns). In reality, it is possible to process only one quadrant to get the whole spectral information because the other angle differs by 90°.

The angle is therefore calcalulated from the first quadrant according to the equation (38) [20]. The variables *X* and *Y* and ***ω*** from the equation are visualized in *Figure 32*.

$$arctan\left(\frac{Y}{X}\right) = \omega\ [rad] \tag{38}$$

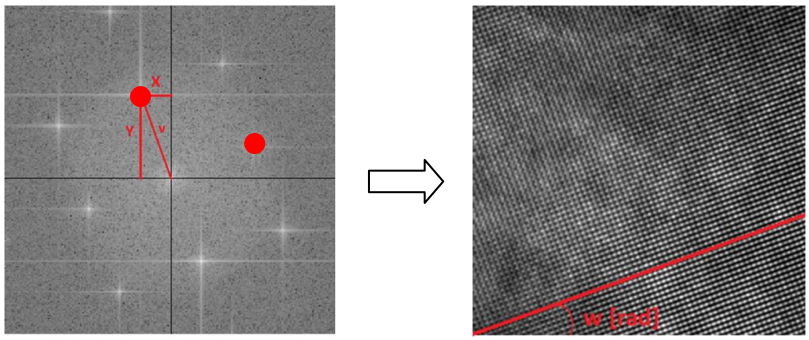

Figure 32: Determination of the tilt of atomic lines from amplitude spectrum

A variable *v* on *Figure 32* represents a spatial frequency and can be calculated as follows:

$$v = \sqrt{X^2 + Y^2}, \tag{39}$$

Inversion of this variable and multiplication by the image size *M* gives a period *T* roughly representing the spacings (in pixels) between the atomic lines:

$$T = \frac{1}{v} \cdot M, \tag{40}$$

The fixed image is initiated as a matrix of zeros and then filled with white lines created in *for* loop. The spacings between lines equal to the period *T* which can be used instead of the lattice constant 0.204 nm (the creation of fixed image is thus automatical for all input image sizes). To better imitate the atoms, the binary grid is blurred by the Gaussian filter (using *fspecial* and *imfilter* command) and the intensities are converted to the full range by the

mat2gray command. Finally, the image is rotated by angle $\boldsymbol{\omega}$ and the fixed image is completed. The procedure is schematically shown in following diagram (*Figure 33*):

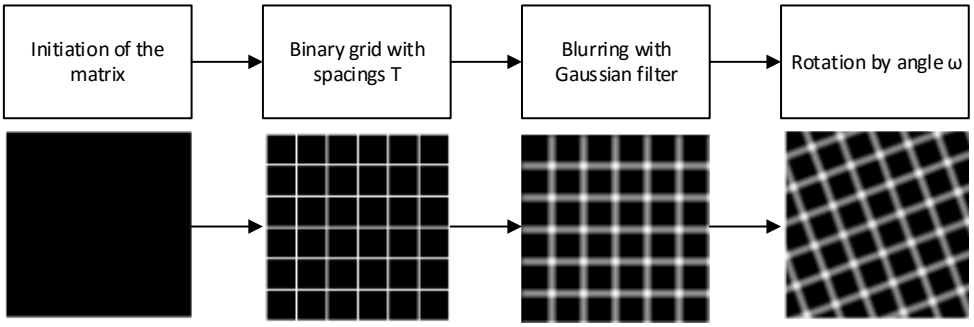

Figure 33: Creation of the fixed image

Accordingly, the moving image and the corresponding fixed image can look like in *Figure 34* (here on cropped images). The white "nodes" in the grid assimilate the appearance of the real atoms. The size of the node is given by the Gaussian filtration. Fixed image in *Figure 34* was created with the Gaussian filter of size 5×5 and 1.2 as the standard deviation.

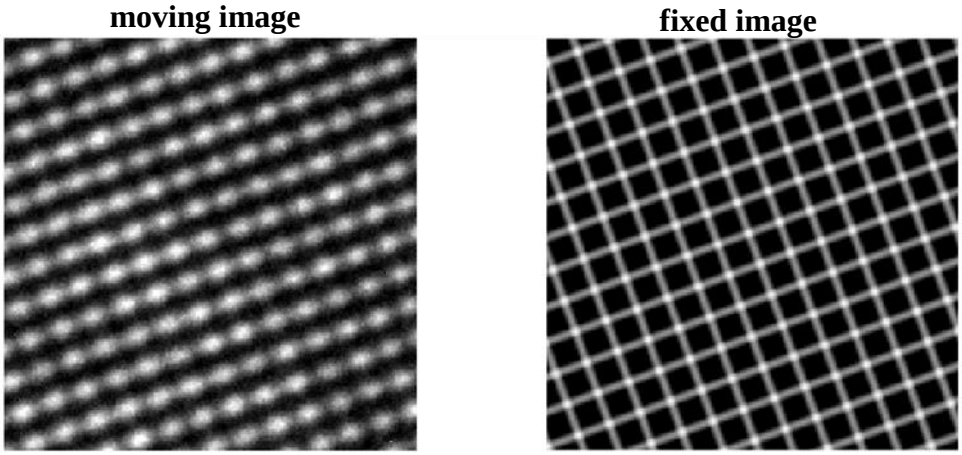

Figure 34: The moving and fixed image to undergo the image registration

5.4 Geometrical transformation

A geometrical transformation best simulating the image distortion caused by the electron optics of the microscope is a nonlinear flexible polynomial transformation of the third order. The higher order polynomials are negligible for the purpose of this work.

Regarding the question of locality or globality of the function, taking into account not extremely big picture but a picture of adequate size, the polynomial function can remain global and spatially invariant.

The third order polynomial transformation of coordinates can be described by the following equations:

$$x' = a_0 + a_1 x + a_2 y + a_3 xy + a_4 x^2 + a_5 y^2 + a_6 x^2 y + a_7 xy^2 + a_8 x^3 + a_9 y^3, \quad (41)$$

$$y' = b_0 + b_1 x + b_2 y + b_3 xy + b_4 x^2 + b_5 y^2 + b_6 x^2 y + b_7 xy^2 + b_8 x^3 + b_9 y^3, \quad (42)$$

A table overview of simulated transformations was created in order to understand how all of these coefficients influent the image (*Table 2*). With a_1 and b_2 equal 1 and other 0, the transformed image should be identical to the original. Simulating the other transformations in separate, a_1 and b_2 always rest equal 1. For example, simulating the impact of a_3, the equations would be:

$$x' = 1 \cdot x + a_3 xy, \quad (43)$$

$$y' = 1 \cdot y \quad (44)$$

The simulation of the coefficient impact (in *Table 2*) was done on a picture created in Matlab as a 2D sine function summed for both directions (*Figure 35*):

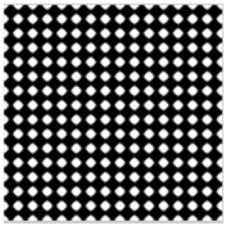

Figure 35: The original image for the simulation

The coefficients in the *Table 2* are related to the equations (41) and (42). The individual impact of the coefficients was modelated. There is always a positive and negative value of the coefficient except of a_1 and b_2 (scaling), where positive value means a value smaller than 1 and negative value means value bigger than 1.

Table 2: Simulated transformations with coefficients in the separate form

coefficient	positive value	negative value	coefficient	positive value	negative value
a_0	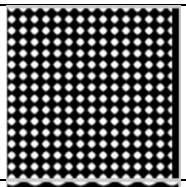	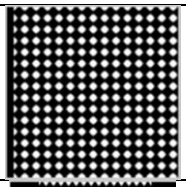	b_0	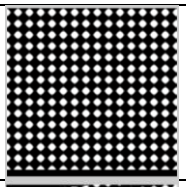	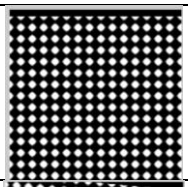
a_1	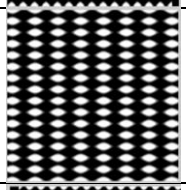	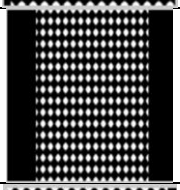	b_1	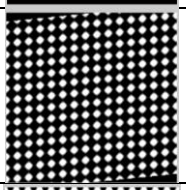	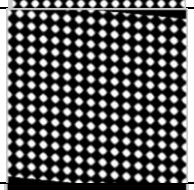
a_2	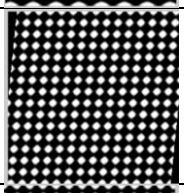	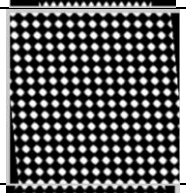	b_2	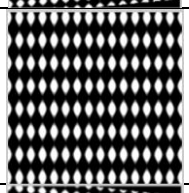	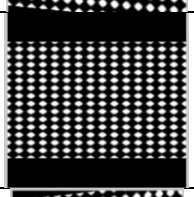
a_3	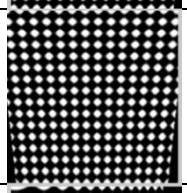	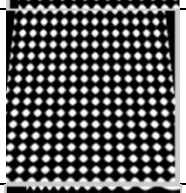	b_3	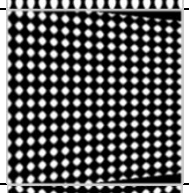	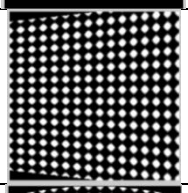
a_4	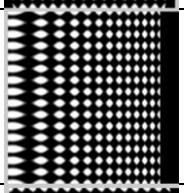	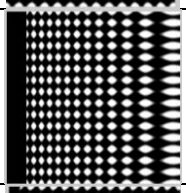	b_4	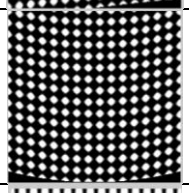	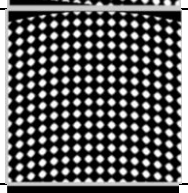
a_5	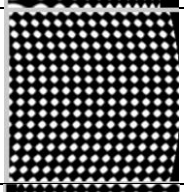	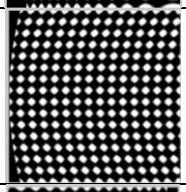	b_5	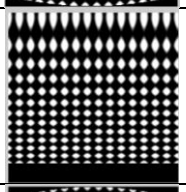	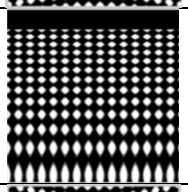
a_6	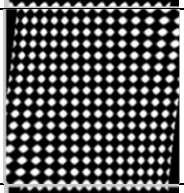	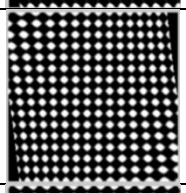	b_6	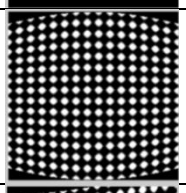	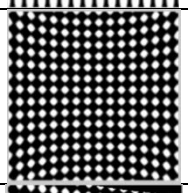
a_7	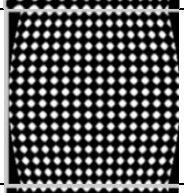	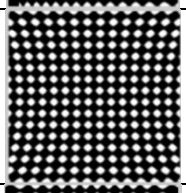	b_7	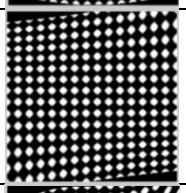	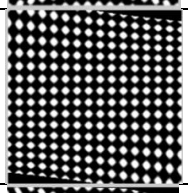
a_8	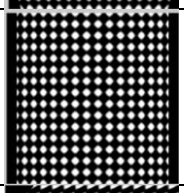	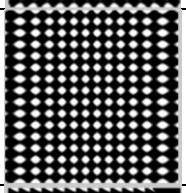	b_8	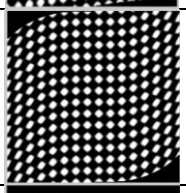	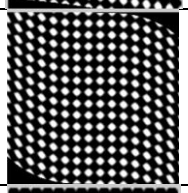
a_9	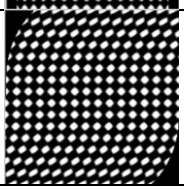	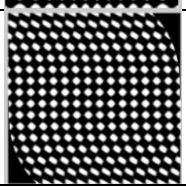	b_9	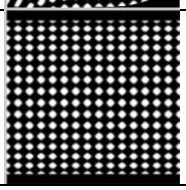	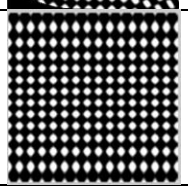

Knowing the impact of these coefficients, it is therefore simple to connect them approximately to the specific optical aberrations (*Table 3*).

coefficient	**impact**
a_0, b_0	shift
a_1, b_2	scale
a_2, b_1	shear
a_3, b_3	projection
a_4, b_5	coma
a_5, b_4	arching
a_6, b_7	shear (squared)
a_7, b_6	distortion
a_8, b_9	shrunk / dilatation
a_9, b_8	curvature

Table 3: Impact of the coefficients to the image

This classification is useful because it enables to set the limits of coefficients and thus restrict the searched space. Setting the limits considerably reduces a time required for image registration. Some of the coefficients can be limited more and some less.

Referring to *Table 3*, the shift (a_0, b_0), scale (a_1, b_2) and shear (a_2, b_1) are certainly present and their correction helps to roughly register the images. Another effects definitely come from the distortion (a_7, b_6) and slightly also from arching (a_5, b_4), curvature (a_9, b_8) and coma (a_4, b_5). The rest of the coefficients (a_3, b_3, a_6, b_7, a_8, b_9) should be much more limited or even excluded from the searched space because such aberrations are not expected on image from TEM.

The limits for the searched space in *Matlab* code were heuristically set according to these observations.

5.5 Criterion function

This type of image registration uses a multimodal approach due to the artificially created model grid as a fixed image, which implies the mutual information as a criterion function. On the other hand, there was a maximum effort to assimilate the two images also on the intensity basis (see *Figure 34*), so the intensity based criteria could also give good results.

There were four different types of criterion function tested – sum of squared differences (SSD), correlation coefficient (CC), cosine criterion (Cos) and mutual information (MI). A simulated optimization of a population of 80 individuals showed that all functions are convergent in terms of shrinking the population among an individual with the best quality (*Figure 36*) and that the time requirements are comparable for all functions except for MI (*Figure 37*) which takes much more time. After all, the **SSD** was chosen as the major criterion function for this registration task because of the short time and better results (than CC and Cos) experimentally determined by the visual inspection of the registered images.

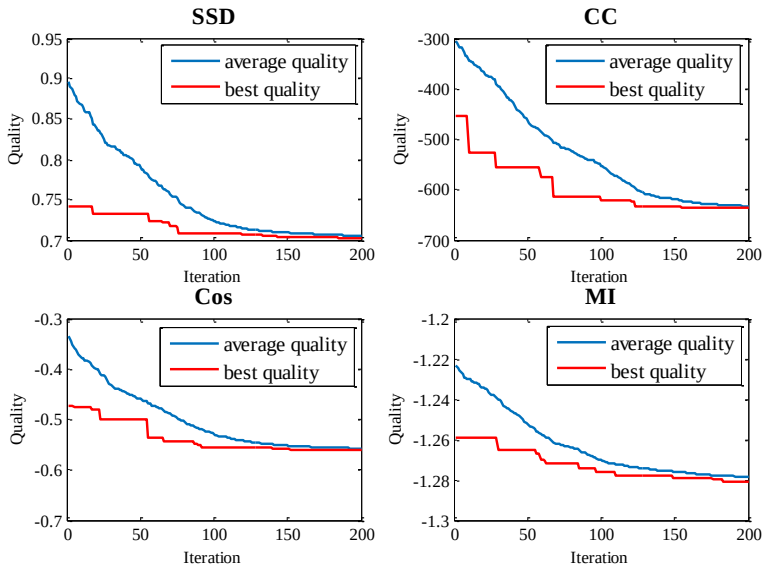

Figure 36: Convergence of different criterion functions during optimization

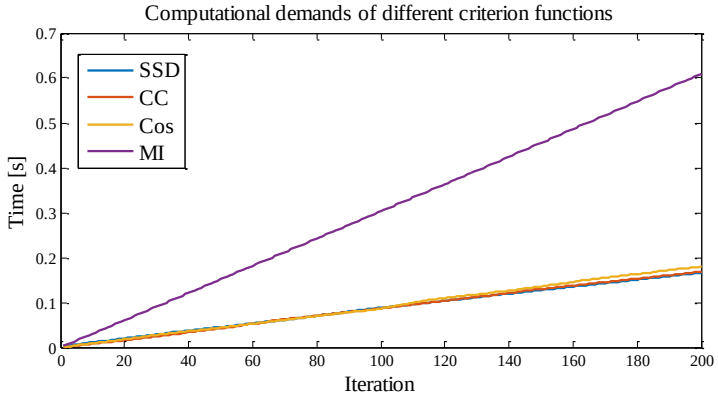

Figure 37: Computational demands of different criterion functions during optimization

5.6 Interpolation

A choice of an interpolation method in a process of image registration is an important step in order to achieve a good quality of the resulting image (which doesn't differ from the original too much) and in order to get the result in adequately short time.

A Matlab function *interp2* can be used for this purpose. The function requires an input parameter defining the type of interpolation, which can be *'nearest', 'linear', 'cubic'* or *'spline'*. Simulation of all of these interpolation methods is shown in *Figure 38*. The *nearest* method is not preferable because the image contains some pixels with intensities abruptly differing from the neighborhood. The *linear* method seems to blur the image too much. The *cubic* and *spline* methods have a risk of possible artifact creation due to the oscillations to the negative values. Nevertheless, the methods both give results of a satisfactory quality and the images are visually similar to the original image.

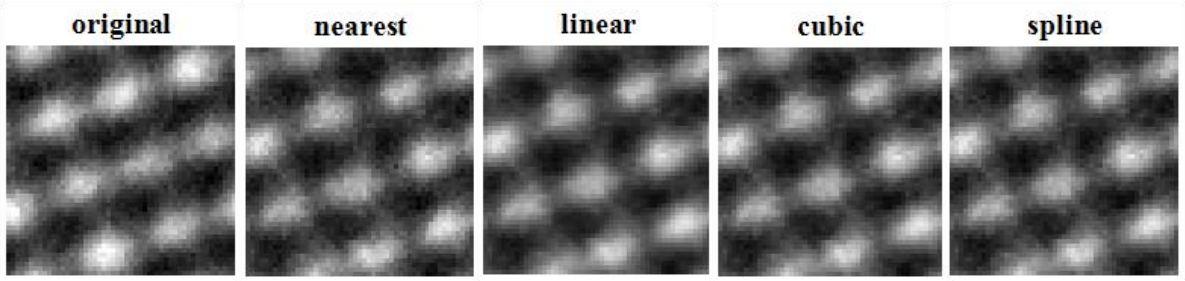

Figure 38: Interpolation of the original image by different methods

Looking at the computational demands of these methods, comparing the dependence of the time needed to perform the interpolation and the size of the input picture (*Figure 39*), it is evident that the *spline* interpolation takes much more longer than the rest of the methods. The *nearest*, *linear* and *spline* methods have almost comparable trend. Evaluating these impacts and assuming that there are no big differences in terms of functionality of the registration, the preferred interpolation method for this task is the **cubic interpolation.**

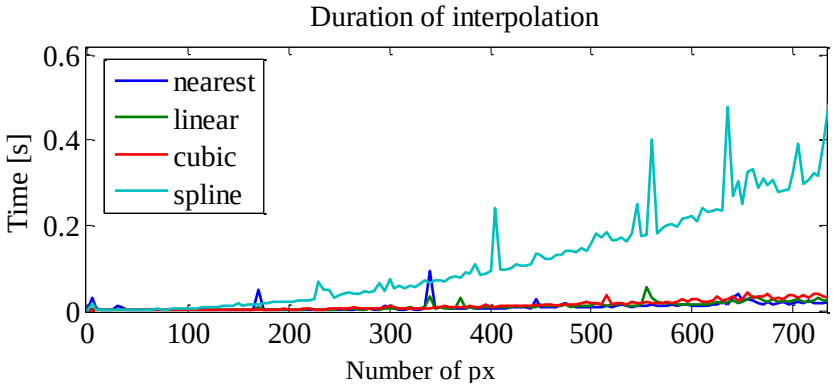

Figure 39: Duration of interpolation depending on input image size

5.7 Optimization

An optimization method is an important element of image registration. A choice of optimization method in this work was done with respect to the type of data, computational requirements, a speed of convergence and ability to avoid a local optimum.

A parameter to be optimized in this work is a vector of 20 coefficients defining a polynomial transformation of the third order. This vector of 20 coefficients represents an individual in a population. The population is gradually shrinking among the optimal solution during the optimization. An initial estimation of the population is done by *random population search*.

In terms of computationally demands, the most of time is consumed by a block with *geometrical transformation* present always if the new individual is generated and its quality calculated. The deterministic algorithms are not suitable because of intolerable computational demands. The genetic algorithms were also rejected, because the quality recalculation of the whole population is present in every iteration of the optimization. So a CRS algorithm was proposed as the major optimization method because only one individual is replaced in the population in one iteration. To avoid entrapment in a local optimum, the CRS is combined with simulated annealing (SA). The convergence in the end of optimization may be very slow, because the solution is optimized in all 20 dimensions. There is therefore a Gradient descent method that could improve the solution in only some selected dimensions. The Gradient descent has as a starting point the best individual from the CRS+SA algorithm. In every iteration, the numerical approximation of first derivation is evaluated and the point in the direction of the biggest gradient becomes the next state. A local optimum should be reached.

The whole algorithm is globally represented in *Figure 30*.A design of this hybrid algorithm was remotely inspired by work combining the simulated annealing and iterative closest point algorithm in [35]. Chapters 5.7.1 and 5.7.2 describe in more detail the *random population search* and the *CRS + SA* method.

5.7.1 Random population search

A **Random population search** is used to create an entry population for a further optimization by CRS. The *random population search* is for this purpose slightly modified from the usual *random search*. It isn't a loop constantly generating a new solution and memorizing the best one. There is a direct generation of a random population connected with filtering of this population. Firstly, M random individuals are generated (using command *rand* and predefined parameter limits) and their qualities are calculated. Consequently, N<M of these M individuals sorted by their quality are chosen to form an entry population for CRS. The process is visualized in *Figure 40* with M=200 and N=80.

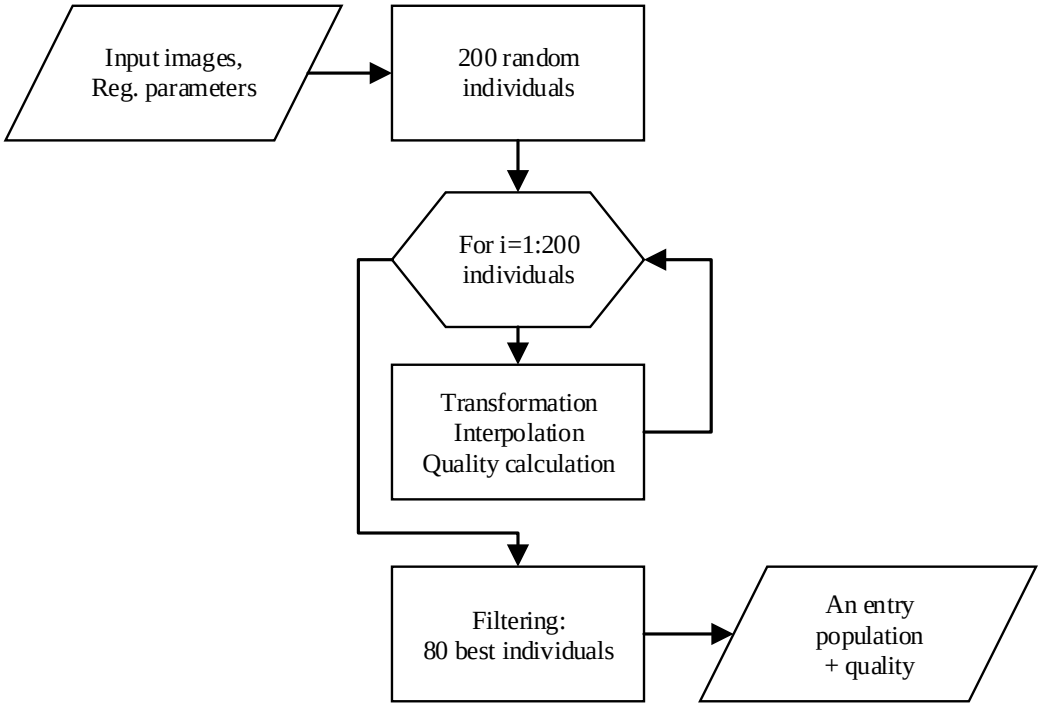

Figure 40: Random population search

5.7.2 CRS and SA

The population created in previous step enters to a **Controlled random search** algorithm. In every iteration, the worst individual from the population is indicated as W and the best as B. Consequently, a Simplex is generated. A Simplex is a set of 21 points (individuals) in a 20-dimensional space. In this case, a simplex always contains the B point. A new point is generated using randomized reflexion according to the description in 4.3.4.

The newly generated point must belong to the searched space. For this purpose, there is a "mirroring" *for* loop that inverts the point into the searched space (given by limits) by individual dimensions successively. This point is used as a set of parameters for transformation of the fixed image followed by the interpolation and quality calculation. If the quality is better than the quality of W, the new point automatically replace the W point and the optimization continues. If not, the new point may still replace the W point and the optimization can therefore escape from a local optimum. It is the effect of **Simulated annealing**. The possibility of accepting the new point decreases with temperature (and the temperature decreases with iteration cycle). The end condition is the number of iterations. The whole algorithm is visualized in *Figure 41*.

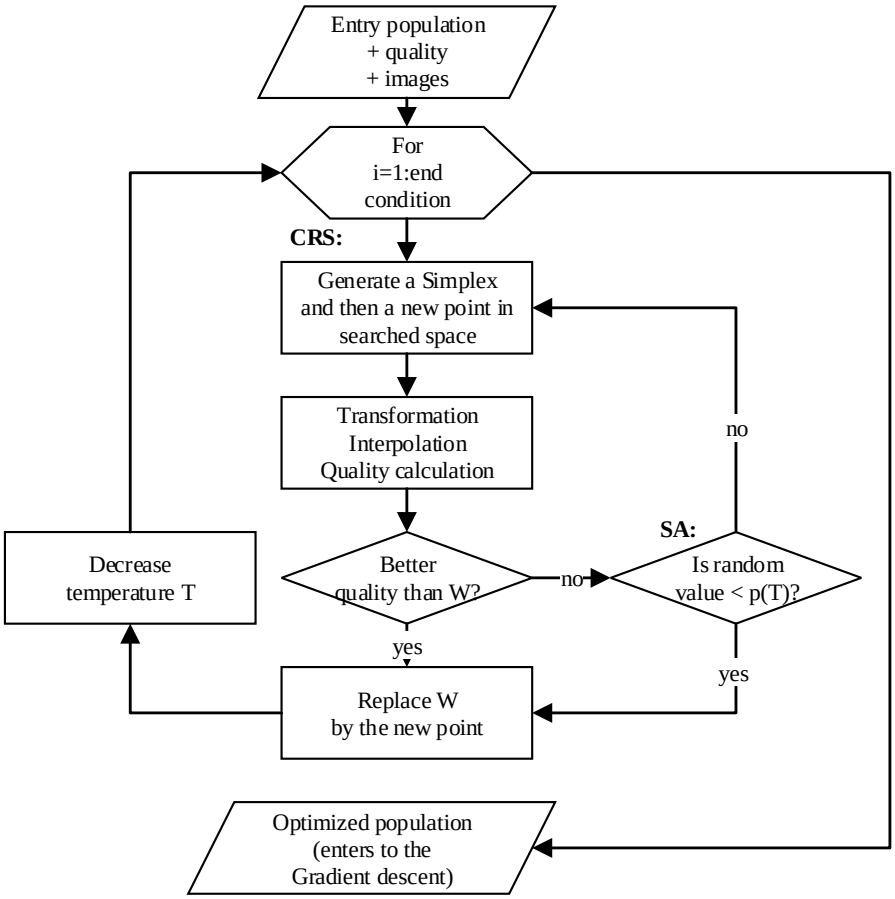

Figure 41: CRS + SA algorithm

6 TESTING ON SIMULATED DATA

6.1 Initiation of images

A *moving image* (that imitates an image from TEM) is created as a 2D harmonic function of size *M=200* and spatial frequency *v=20*. The function is first created in both directions and then summed in order to form a regular grid with white "atoms" in the nodes. The moving image is then geometrically transformed using a polynomial transformation with following coefficients:

$$x' = a_1 x + a_7 x y^2, \tag{45}$$

$$y' = b_2 y + b_6 x^2 y, \tag{46}$$

where $a_1 = 1,\ a_7 = 2 \cdot 10^{-5},\ b_2 = 1,\ b_6 = 2 \cdot 10^{-5}$. A cubic interpolation method was used. The coefficients were chosen in order to simulate a visible barrel distortion. The image is therefore distorted only by 2 coefficients (a_7 and b_6) and the optimization is also 2-dimensional, because there is a heuristic supposition that this distortion would be eliminated by a geometrical transformation with negative a_7 and b_6 coefficients simulating a pincushion distortion (but with different values). A reason of the dimension restriction for this testing is that the graphical results showing the process of optimization would be clearer in 2D.

A *fixed image* is created as a grid with spacings *T=M/v* with an application of blurring filter (as visualized in *Figure 33*). Both images are shown in *Figure 42*.

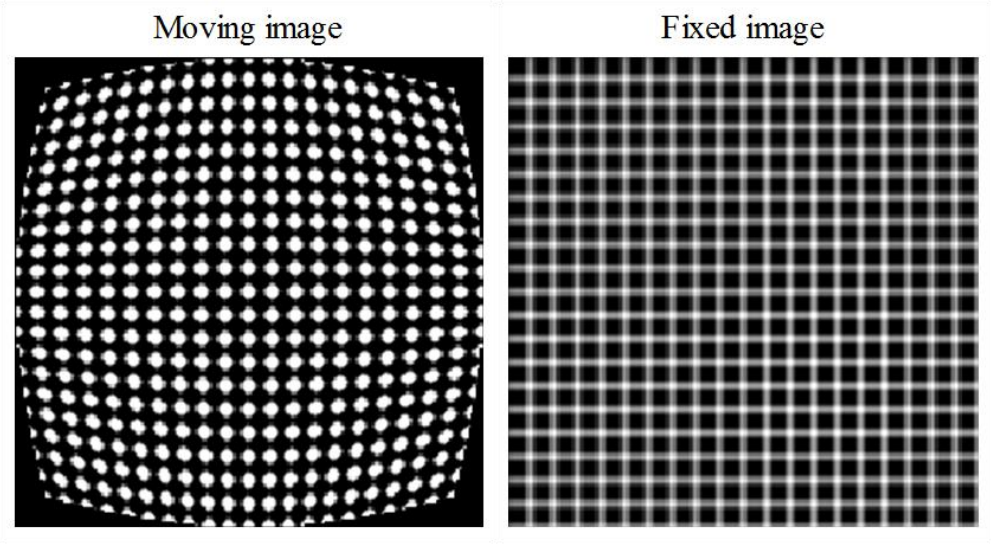

Figure 42: Simulated moving image with barrel distortion and a fixed image

6.2 Process of registration

A searched space for image registration is restricted by limits from $5 \cdot 10^{-5}$ to $5 \cdot 10^{-5}$ for both coefficients, the criterion function is SSD and the interpolation method is cubic. A first step is a random estimation of coefficients by *random population search*. A population of 60 individuals is created and then reduced to 30 individuals in accordance with the best quality (the lowest values of SSD) - *Figure 43*.

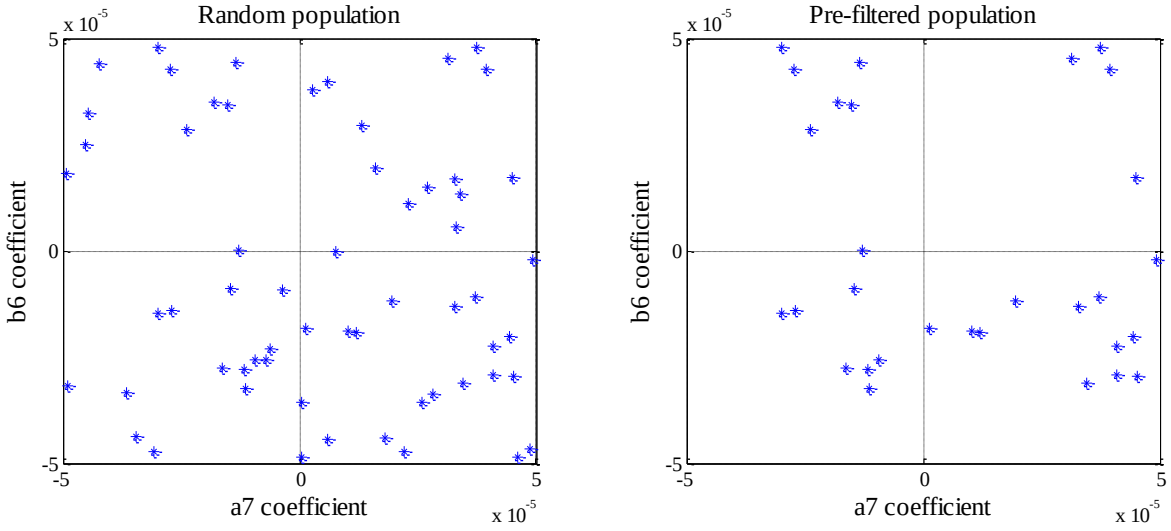

Figure 43: Random population search

The pre-filtered population enters into the *CRS+SA* optimization with 150 iterations. An initial temperature T_0 for *SA* is 0.005. The setting of T_0 was made with respect to the range of the searched space, number of iterations and behavioral observations. In sum, the SA is accepted in around 8 cases of 150 registration cycles. The population shrinking among the optimal solution during the registration is visualized in *Figure 44*.

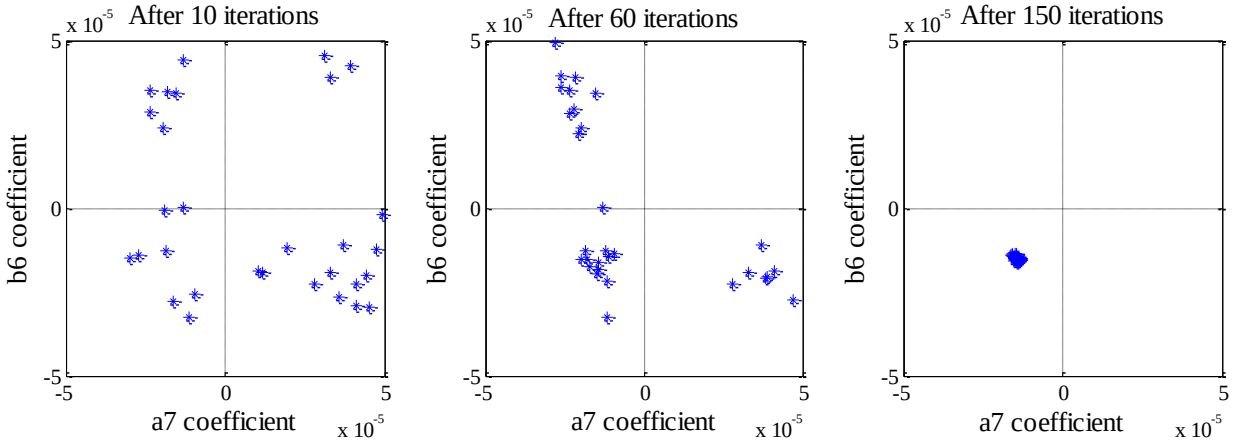

Figure 44: Optimization of population during the image registration

The average quality in population continuously descends during the optimization. The small fluctuations upwards are caused by the SA effect. The best quality belonging to the best individual in the population is also descending during the optimization – see *Figure 45*.

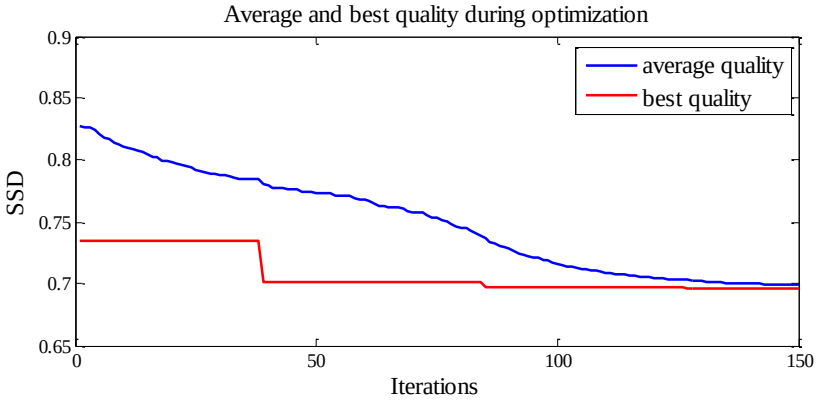

Figure 45: Quality during optimization in registration process

The optimization continues by the *Gradient descent*. The best individual from the last generation becomes the start point for the gradient method. A parameter *h* defining a small neighborhood for derivation is $5 \cdot 10^{-12}$ and a step of method *alpha* is $5 \cdot 10^{-11}$. After 20 steps, the gradient method improves the solution and also its quality – *Figure 46*.

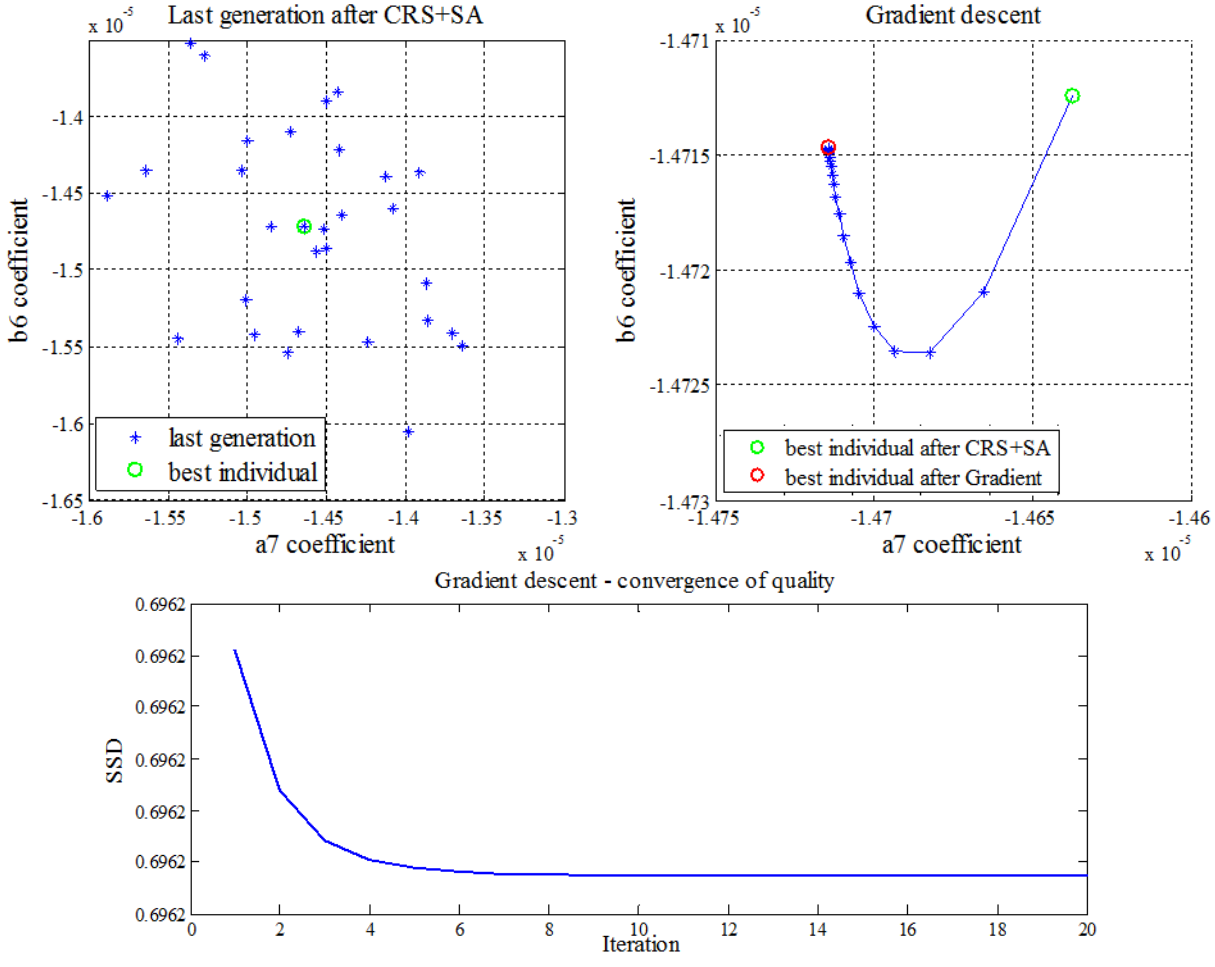

Figure 46: Gradient method

6.3 Results

The final optimal solution for the geometrical transformation is $a_7 = -1.4714 \cdot 10^{-5}$ and $b_6 = -1.4715 \cdot 10^{-5}$. This transformation is applied on the moving image and a corrected image appears (*Figure 47* – left). The visual appearance of the result is good. There are only small imprecisions in the edges of the image. An accurate option how to evaluate quality of registration is by overlapping the two images (corrected and fixed) in different colours - *Figure 47* – right. The fixed image is shown as a red component and the corrected image is a green component of the resulting image. The well overlapped points are then displayed in yellow.

Corrected moving image Overlapping of corrected and fixed image

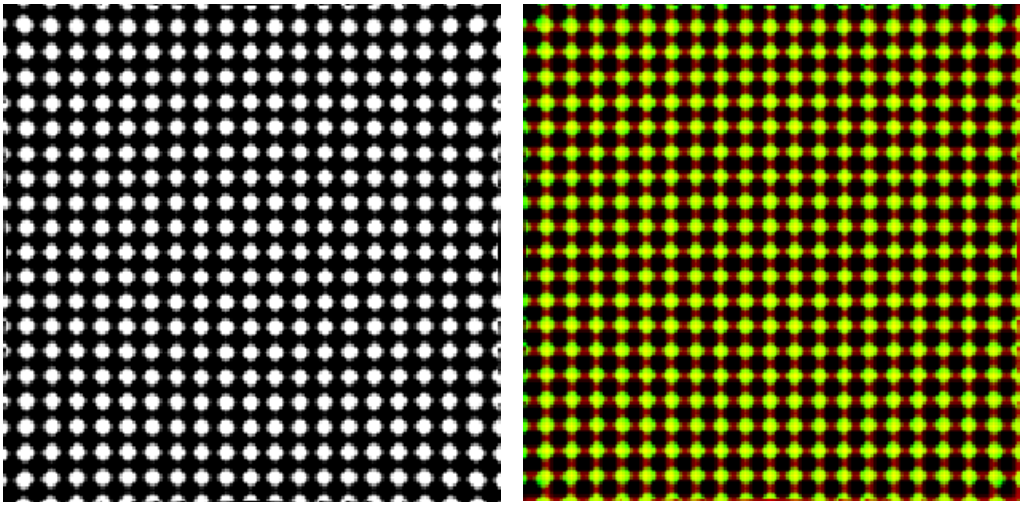

Figure 47: Corrected moving image and overlapping of corrected and fixed images

A detailed examination of the overlapped images shows that there is a constant shift by around 1 pixel in the 4 "atoms" located at the corners of the image. However, this phenomenon doesn´t influence the total quality of registration. There must always be a presumption of imperfectly registered borders because of lack of surrounding pixels. It must be taken in account for further registration. A good solution would be cropping of these border pixels before the end of registration.

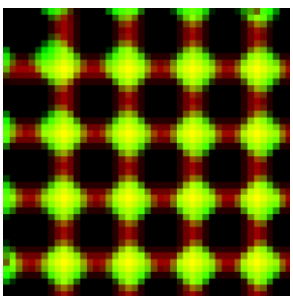

Figure 48: A detail from overlapping images (left top corner)

7 TESTING ON REAL DATA

7.1 Algorithm modification

The registration algorithm itself is very similar to the algorithm applied on simulated data. One of the differences is the "preparation" of the fixed image. The fixed image must be rotated in order to correspond with the tilt of atomic lines in the moving image (principle described in chapter 5.3.2). An advantageous thing is that the rotation angle doesn´t have to be detected with extreme precision, because it will be adjusted by optimizing the parameters representing tilt (a_2 and b_1). Moreover, the tilt optimization in each direction separately can be even beneficial, because the microscope could have been affected by not correctly set orthogonality and the registration can correct it.

Another difference is in the dimensionality of the searched space. There are now 20 parameters to be optimized in contrast with 2 parameters with simulated data. Such a multidimensional optimization with big images is very time-consuming and the convergence to the optimal solution is slow. The optimization algorithm was therefore slightly modified in order to reduce the time requirements. The main optimization block (CRS+SA) is realized as a multilevel (bi-level) optimization.

There are two consecutive blocks of optimization. In the first one, the moving and fixed images are cropped and only small parts of these images (e.g. 60×60 px taken from the center) enter to the registration block. The searched space is only 6-dimensional (a_0, a_1, a_2, b_1, b_2, b_3) in order to optimize the most misaligned coefficients (scale, translation and shear). After this first block, the second one follows. In this block, a flexible image registration in 20 dimensions is performed on the whole input images (256×256 px). The searched space for the 20 coefficients is restricted into set limits. Only the 6 coefficients from the first block of optimization are restricted much more in order to remain in a small neighborhood of the first-block´s outputs. (For example, the limit for translation in x-axis in the first block was <-8 px,8 px> and the best registration was in position about 6 px. In the second block, the limits are <5px,7 px>). The bi-level registration is illustrated in *Figure 49*.

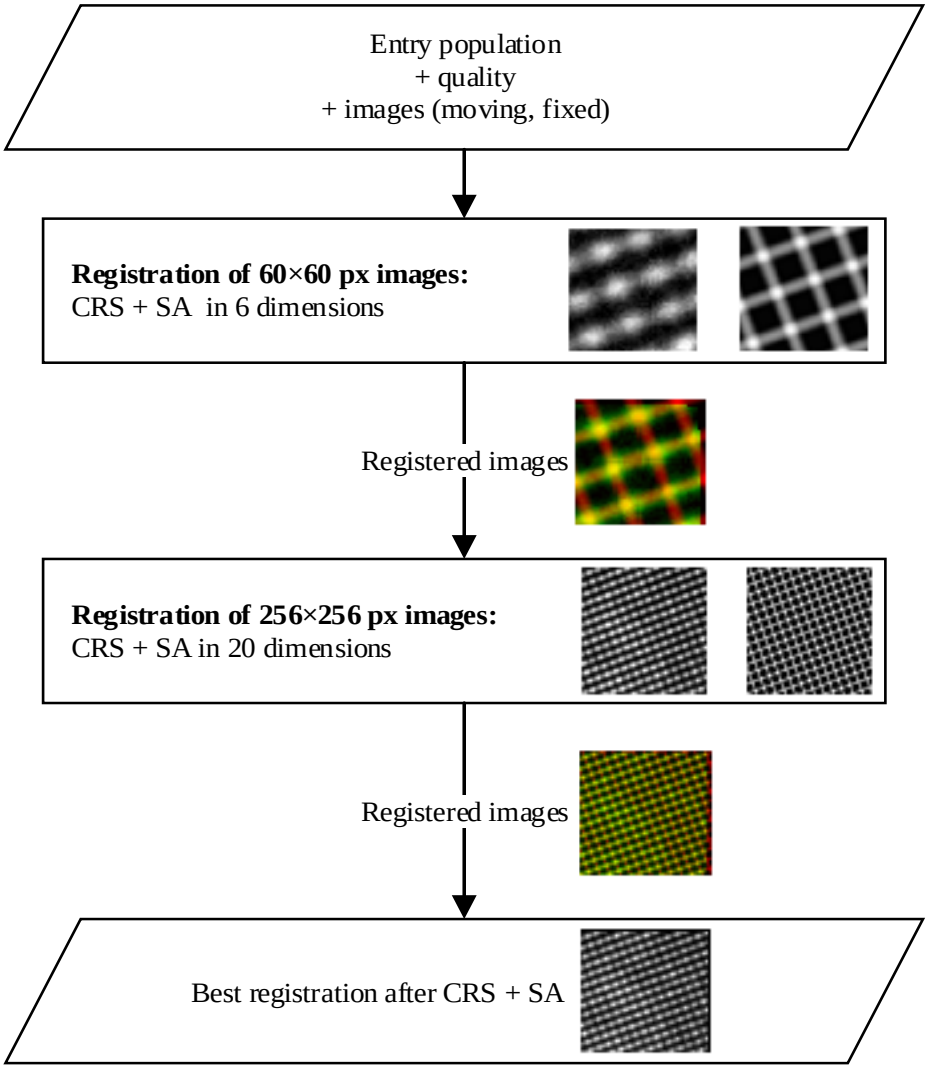

Figure 49: Bi-level image registration on real data

Concerning the following gradient descent block, the principle remains unchanged. The gradient method refines the solution by optimizing two coefficients representing the distortion (a_8 and b_7). The result providing the best quality is designated as the final solution. The moving image can be corrected from the distortion.

7.2 Code description

The main script is called *MAIN.m*. This script contains the editable parameters and the loading of input image. All other functions are called through this script. There are functions *geom_transf.m, quality.m* and *registration.m*. The registration starts after pressing the start button from the *MAIN.m* script. The results are then visually presented in graphics.

7.3 Results – main images

7.3.1 Set of images

A set of images acquired by the TEM contains in total five images of visually acceptable quality. These images are of size 1024x1024 px. Such big images are not suitable for registration, because it would be too computationally demanding. Each 1024x1024 px image was therefore divided into 16 sub-images of size 256x256 px (*Figure 50*). Some of the sub-images were excluded from the set of main images and classified as degraded (more in 7.3.3). There are therefore in total 66 images to be tested by the registration algorithm. Such amount of data creates a good basis for the further algorithm's robustness evaluation. Number of iteration for the first run of optimization was set to 700 and the population size to 100. Number of iterations for the second run of optimization was set to 1500 and the population size to 150. The limits for the searched space were set heuristically.

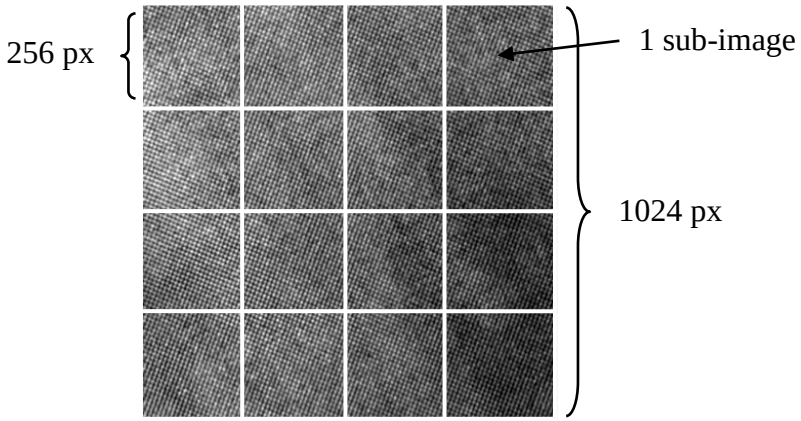

Figure 50: Creation of 16 sub-images from an image coming from TEM

Results

The results of registration are evaluated in terms of the validity and quality of the registration. The aim of the validation is to evaluate the robustness of the algorithm and also to prevent the errors due to the optimization being trapped in the local optimum. There is a lack of golden standards used for evaluation of the registration. The commonly used method for the validation is a visual inspection of the registered images [20], [36]. In this work, the validation was done by the visual inspection of the images created by overlapping of coloured layers. The red layer represents the fixed image and the green layer represents the corrected image. The good registration appears as yellow colour in the nodes (atoms).

The registration was successful in 64 of 66 cases, which makes 97 % of successfully corrected images. An example of one chosen result is in *Figure 51*.

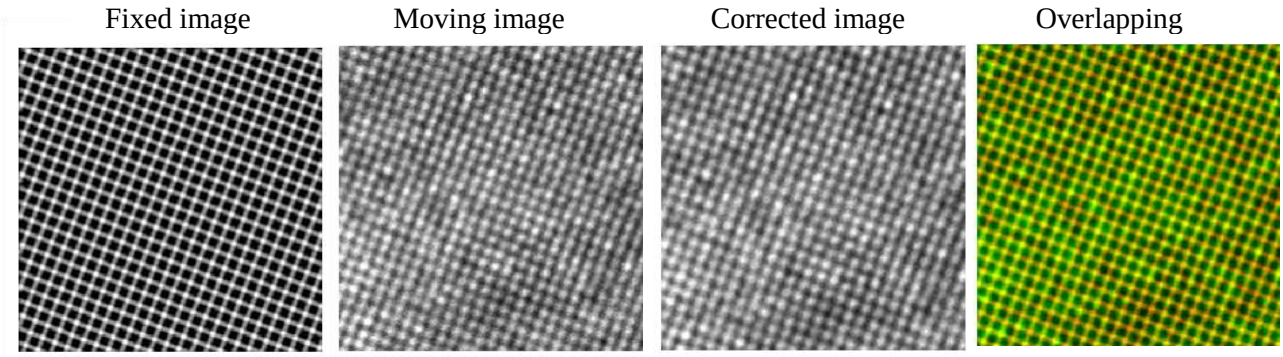

Figure 51: Fixed and moving images, corrected image and overlapping of images

From these 64 images, only 32 images (50 %) were improved in quality by the Gradient descent method. More precisely, two of the five big original images (including 32 sub-images) were probably slightly more distorted (by coefficients a_7 and b_6) than the others, so the gradient method modifying these coefficients had a beneficial effect. The improvement in quality was in a small range (in order 10^{-5} of SSD value) but the trend was purely exponential in all cases (result in *Figure 52* - left). The rest of the images wasn't improved in quality by the Gradient descent (example in *Figure 52* - right). The reason could be in the previously mentioned lack of barrel/pincushion distortion or in not so well set parameters of the gradient method for the given image.

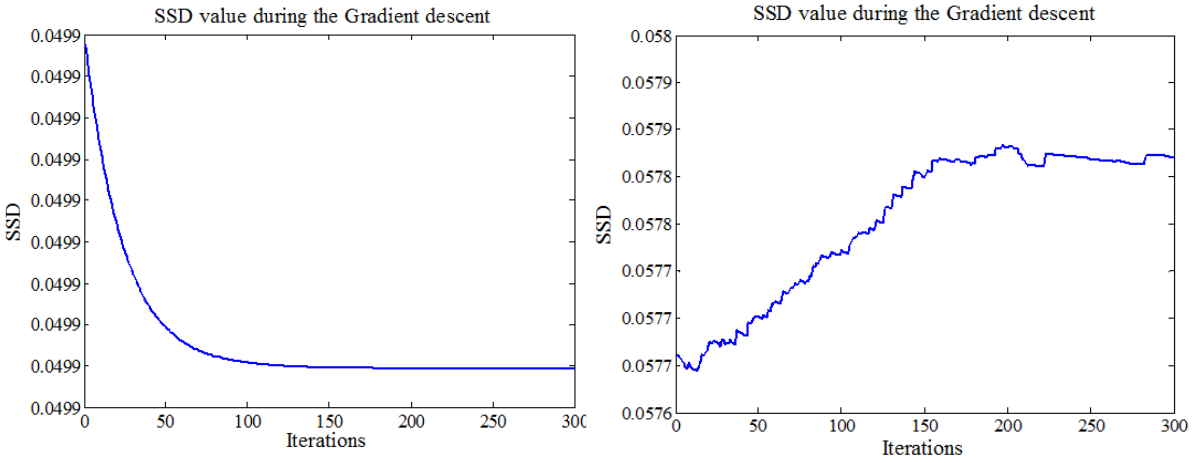

Figure 52: Gradient descent: left –improvement in quality, right – no improvement

Concerning the two images that have not been corrected well, the reason is probably in slower convergence to the optimum. The improvement would consist in the change of number of iterations or in more severe restriction of the limits for the searched space. The first image (*Figure 53* - left) shows only small imprecisions in the top left and right corners, where the atoms (in green) don't fit to the grid (in red) perfectly due to the 1-2 px shift. Second affected image (*Figure 53* – right) is totally mis-registered in one direction. The atomic rows are registered well but the columns are not. This problem has occurred even during the first level of registration (on small 60 px image). It reflects a deficiency of optimization cycles or an entrapment in a local optimum. The initial temperature for SA should be in this case adjusted in order to increase the possibility of accepting worsening step and escape from the local optimum. On the other side, it would prolong the convergence.

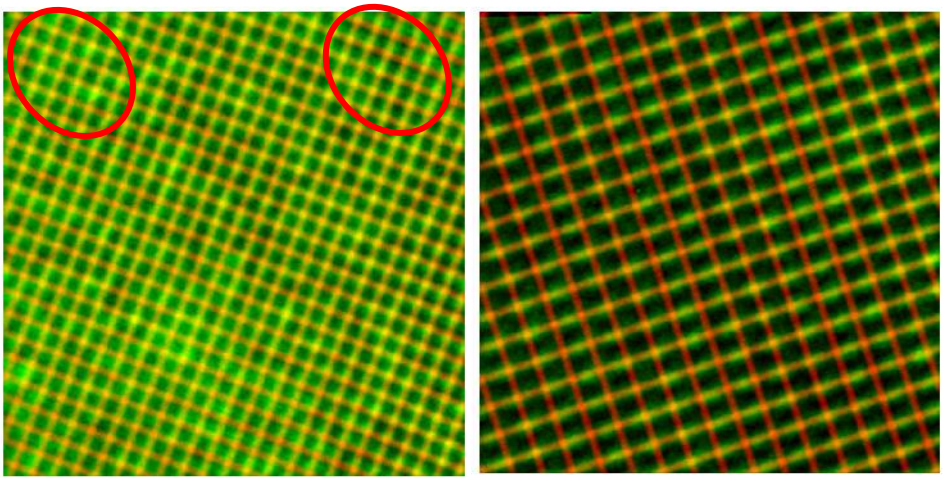

Figure 53: Badly registered or mis-registered images

Coefficients

Concerning the resulting coefficients of the geometrical transformation, the example is in *Table 4*. The combination of these coefficients forms a set of parameters of the geometrical transformation correcting the aberrations caused by the electron optics. It may be assumed that it is the approximation of the inverse polynomial transformation deforming the image.

The impact of the coefficients was presented in *Table 2*. According to the *Table 4*, the coefficients a_1 and b_0 determining the scale in both directions differ by 0.1. The image was probably slightly prolonged in one axis during the image acquisition. And the coefficcients a_7 and b_6 differ by sign, which means that the image was corrected by the „pincushion distortion“ transformation in *x* direction and by the „barrel distortion“ transformation in *y* direction. Neverthless, the conclusion coming from these coefficients of such small images (256×256 px) isn't very meaningful.

Studying of these coefficients isn't simple and is beyond this work. Important is that the algorithm is able to give this type of results for the further possible study.

Table 4: The output parameters of geometrical transformation after the registration

Index	Coefficient a	Coefficient b
0	5.67	$9.1 \cdot 10^{-1}$
1	$9.2 \cdot 10^{-1}$	$1.2 \cdot 10^{-2}$
2	$-2.6 \cdot 10^{-3}$	$9.3 \cdot 10^{-1}$
3	$1.3 \cdot 10^{-7}$	$-1.2 \cdot 10^{-6}$
4	$1.2 \cdot 10^{-5}$	$-8.0 \cdot 10^{-6}$
5	$1.1 \cdot 10^{-5}$	$5.0 \cdot 10^{-6}$
6	$-7.1 \cdot 10^{-8}$	$-2.1 \cdot 10^{-7}$
7	$7.5 \cdot 10^{-8}$	$-3.3 \cdot 10^{-7}$
8	$7.5 \cdot 10^{-8}$	$-5.8 \cdot 10^{-7}$
9	$9.12 \cdot 10^{-8}$	$1.7 \cdot 10^{-7}$

7.3.2 Difference between the direct and the bi-level CRS optimization

Following overview presents a difference between the direct and bi-level CRS optimization (registration). The direct variant registers the whole image in all 20 dimensions at once. The bi-level variant (used in this work) registers the cropped images firstly in 6 dimensions and consequently the whole images in all 20 dimensions. The testing was made with identical conditions in both cases (the same conditions as for testing of the main images).

Direct CRS registration	**Bi-level CRS registration**
Duration*: 39 mins Population quality during the optimization: 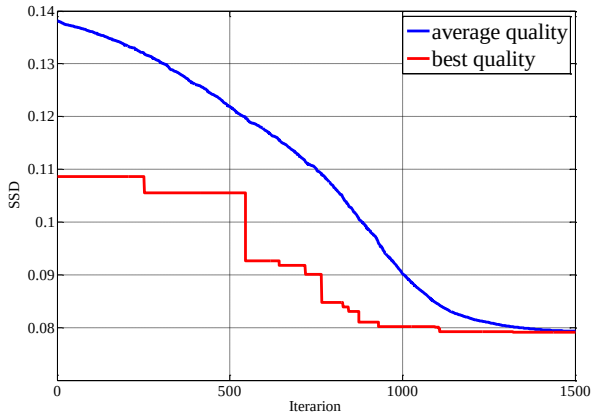 Quality reached: 0.0791 (SSD) Convergence in quality after: 1400 iterations Improvement by Gradient: yes Result: Successful registration 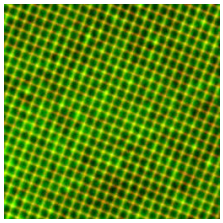 Conclusion: The registration is successful but it is very slow because the 20 parameters are optimized all in once. The distortion coefficients with minimum impact don't make any improvement in the beginning of optimization. The major problem is to find the first approximation of shift and scale in both directions in order to fit to the model grid. The *while* loop generating a new better point by Simplex method was probably many times repeated in the beginning.	Duration*: 20 mins Population quality during 2. optimization run: 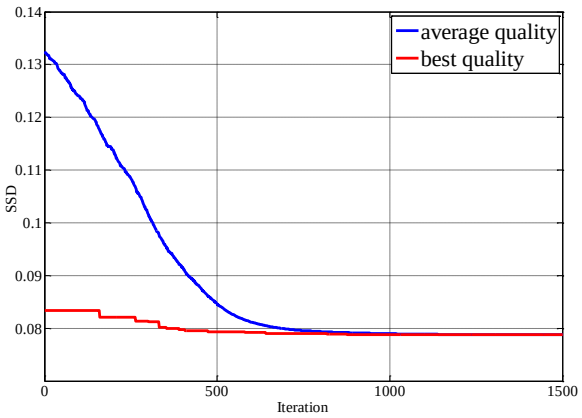 Quality reached: 0.0788 (SSD) Convergence in quality after: 750 iterations Improvement by Gradient: yes Result: Successful registration 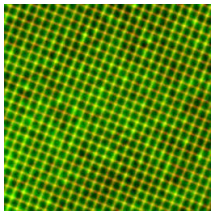 Conclusion: The registration is successful and it took only a half of time than in previous case. The convergence is much quicker because the 6 coefficients of shift, scale and shear are already preset from the first run of optimization. The convergence is attained after 750 iterations. The shorter duration can be explained by less of iteration cycles in *while* loop for generation of the new better point by the Simplex method. So this is the better variant.

* Duration of whole registration process on computer with parameters: processor Intel CORE i5 (2.3 GHz) with 4 GB RAM

7.3.3 Example of big image

The previous testing on 256×256 px images proved the robustness of algorithm, which was mainly the goal of this work. Processing bigger images is very computationally demanding, so it was reduced to the minimum in this work. However, some testing was done and one of the results is presented in this chapter.

Registration of 1024×1024 px image

The input image for registration was of size 1024×1024 px. The registration process was the same as in previous cases, only some parameters were adjusted. The population size for *random population search* before filtering was increased to 1 000 and the number of iterations for both runs of *CRS+SA* optimization was increased too (to 1 500 and 6 000 iterations respectively). The sub-image for the first run of optimization was taken from the center of the big image and was of size 120×120 px. The result after the first run of optimization is visualized in *Figure 54* as overlapping of the corrected and fixed image. The registration in 6 dimensions was successful and the quality attained the convergence after 700 cycles (visualized in *Figure 55*).

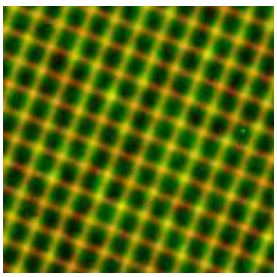

Figure 54: Overlapping after the first run of optimization

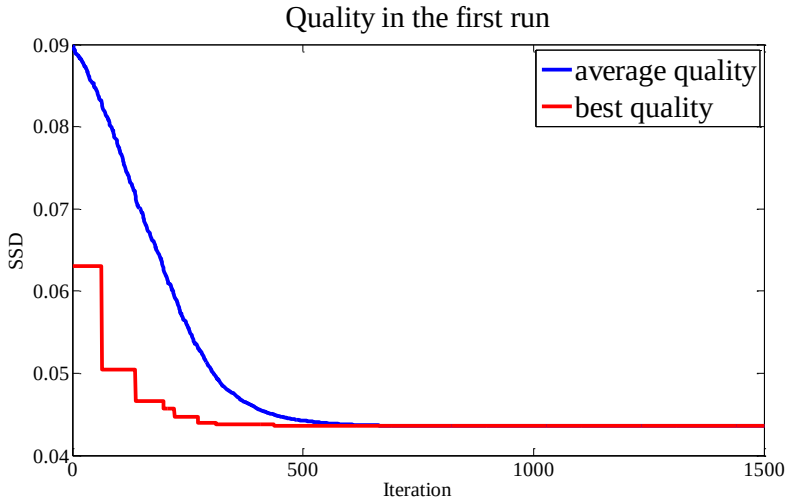

Figure 55: The quality during the first run of optimization

Following *Figure 56* presents the result after the second run of optimization. It is also displayed as the overlapping of the corrected and fixed image. The detail is in *Figure 57*.

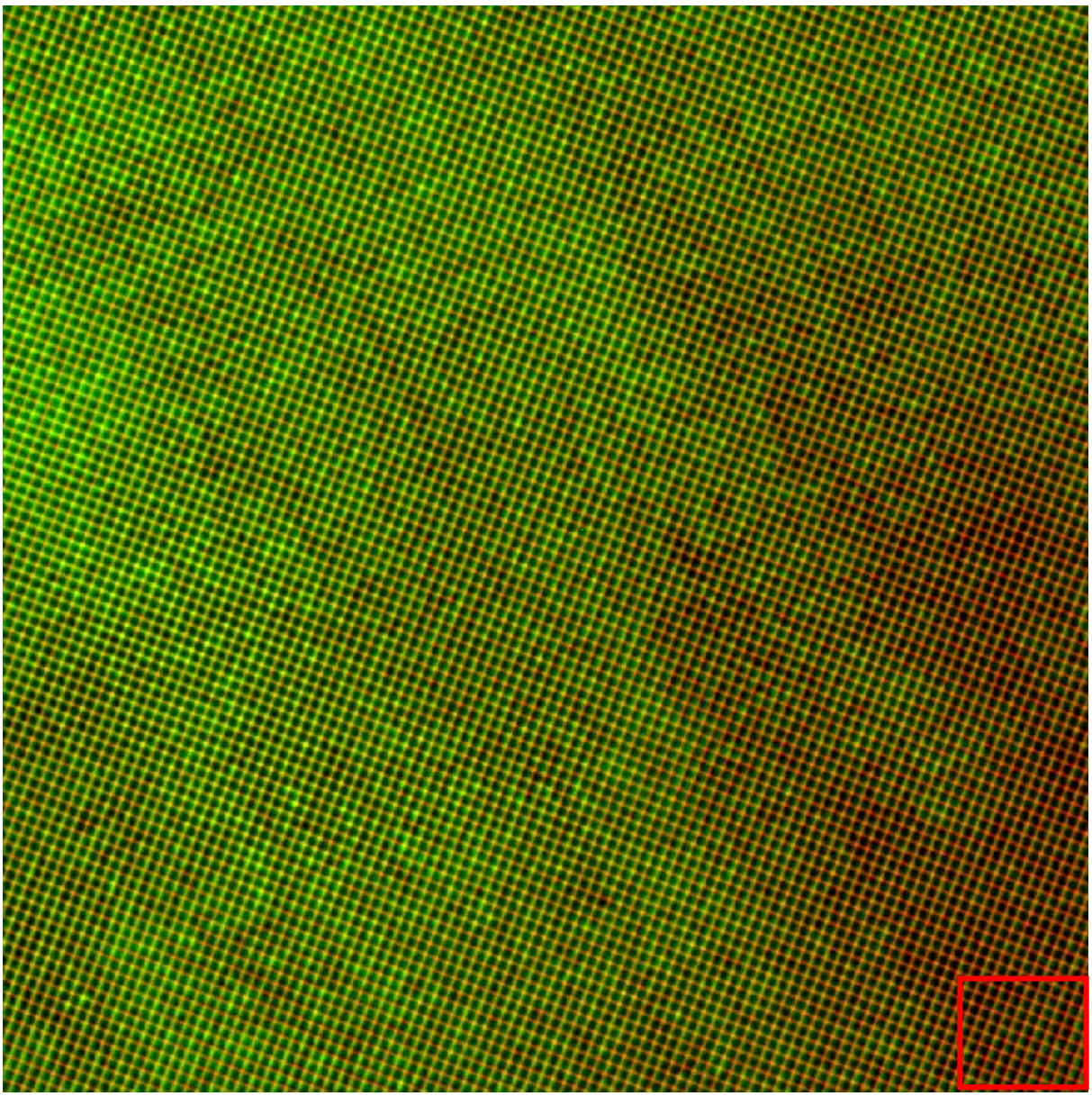

Figure 56: Overlapping after the second run of optimization

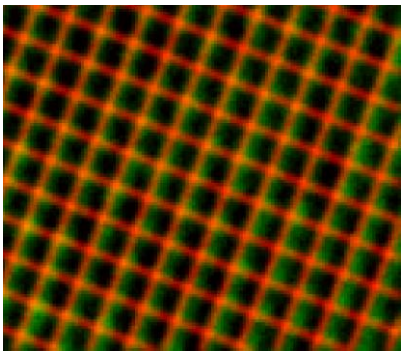

Figure 57: A detail from Figure 56 (from the red square)

The *Figure 56* shows a very good result considering that almost the whole image was successfully registered (the red *fixed image* overlapped with the green *corrected image* is displayed as yellow in the "nodes" presenting atoms). Only the bottom right corner shows some imperfections in overlapping. The detail displayed in *Figure 57* shows the imperfect registration of about 10-12 atomic lines. The shift is present and the differences increase towards the corner. It is apparently the area where the distortion of the original image was bigger and the shadow in image decreasing the contrast was present. The biggest shift in this area is about 4 px. All the other corners were registered successfully except of a small area in the bottom left side, where the shift is also present.

Examining the progress of quality during the second optimization block (visualized in *Figure 58*), it is evident, that the best quality in the population has not been improved during the first 2 000 iterations. The best individual during this phase was probably represented by the state with predefined first six coefficients from the first run of optimization and other coefficients equal to zero. But after the iteration 2 000, the best quality started to improve and the improvement was continuous until the end of registration. The convergence was almost completely attained. The improvement after the iteration 2 000 can be explained in optimization of the coefficients causing the non-linear distortion (coefficients of the second and third order). Maybe the third block of optimization should be present after the second one. This block would optimize only the coefficients of the second and third order. It would lead to the better registration in the corners.

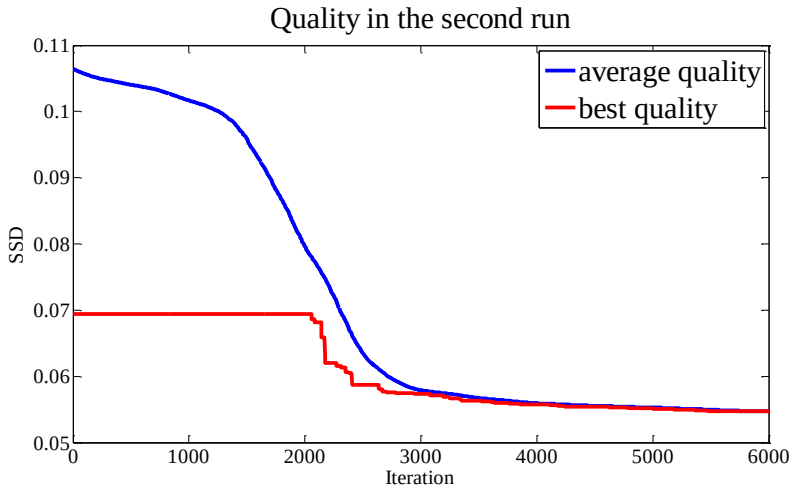

Figure 58: The quality during the second run of optimization

The process of registration of this image took in total 16 hours on computer with processor Intel CORE i5 (2.3 GHz) with 4 GB RAM. A way how to accelerate the convergence should be in the stricter setting of the limits of the searched space.

7.4 Results - degraded images

Another set of images coming from the TEM is formed by images with not so good visual quality. There are visible shadows, noise and surface irregularities. Moreover, the atomic lines are not well recognizable (example in *Figure 59*) – it may be caused by the translucent lower atomic planes due to the surface inequalities. The tested images are of various sizes and magnifications. The testing was performed on 30 selected images.

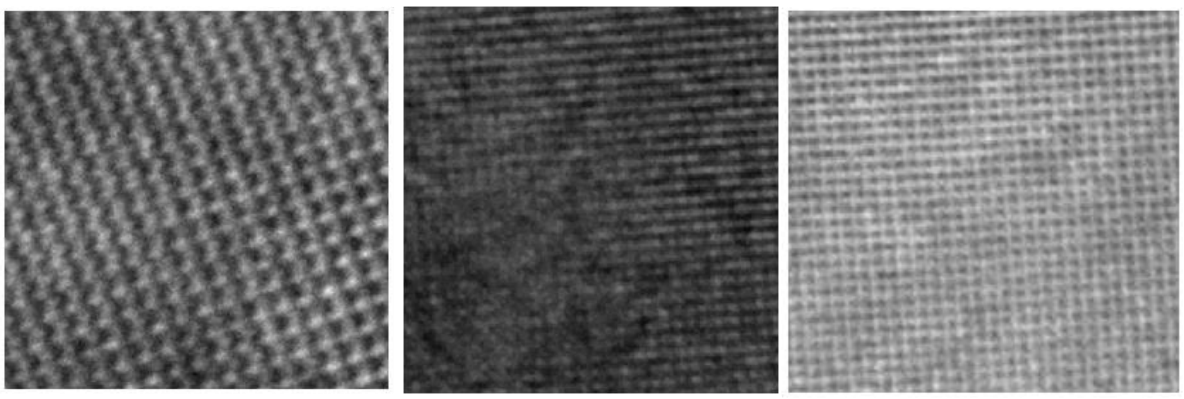

Figure 59: Example of the degraded images

The statistical evaluation and validation of the algorithm is very difficult because every image has a specific noise with individual impacts. The validation of the result was done by the visual inspection of the overlapped images. From the 30 images, the 21 were registered well. It means that the registration was successful in 70 % of cases. The 30 % of images would be probably improved in quality after the further optimization steps because the convergence was not attained completely. The improvement in quality by the gradient method was present only in 10 % of cases. Two of the mis-registered images had badly evaluated angle for the creation of fixed image. The rest of images was very degraded. The details and some representative cases of this testing are present in following pages.

Good registration on slightly degraded image

The moving image represented in *Figure 60* is nice in the top left border, where the atoms and their background are well recognizable, whereas the bottom right corner shows the unrecognizable atoms almost forming the whole lines. Besides that, the registration is successful in this case. The unevenly large black borders on the left and bottom side of the corrected image are probably the indicative of bad orthogonality in the moving image (the vertical shear is bigger than the horizontal shear). The overlapping of images proves the success of the registration.

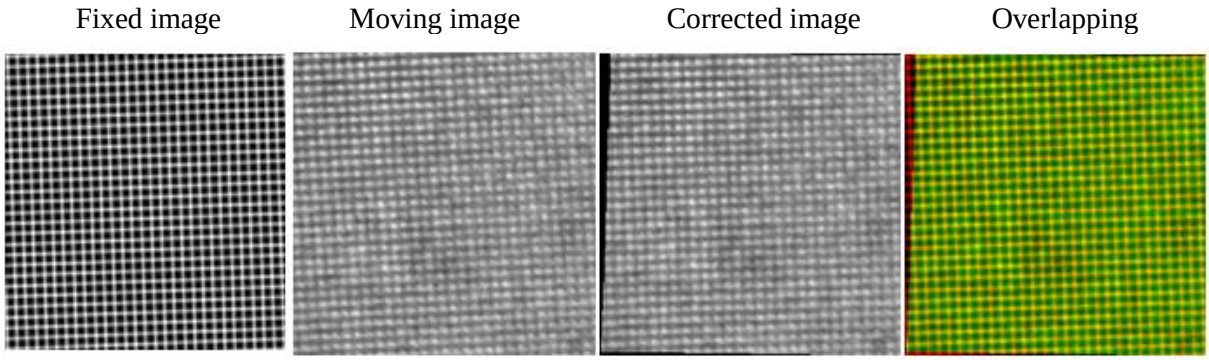

Figure 60: An example of good registration

Good registration on image with translucent lower atomic plane

The atomic lines in the moving image in *Figure 61* seem to be preferential in one direction. It is the impact of astigmatism. From experience, it is not a big problem for the image registration. A bigger fault of the moving image is that the atoms (for example those on top right corner of the moving image) aren't well discernable from the background. The background should be dark, but it is grey almost in the same way than the atoms. It is caused mainly by the translucent lower atomic plane. This translucent plane causes that the spacings between atoms are shown as gray lines. Despite these imperfections, the registration works well, what is proven by the overlapping of images.

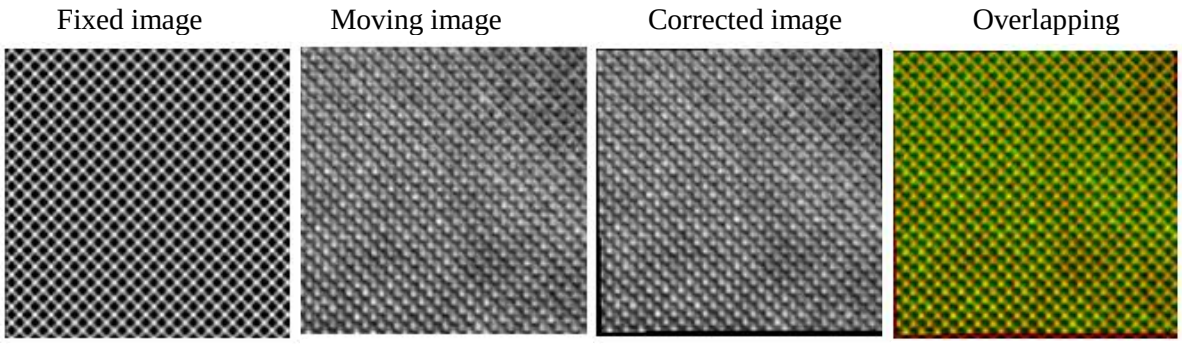

Figure 61: An example of good registration even on degraded image

Bad angle detection

One of the problem that occurred in few cases was incorrect creation of the fixed image. According to the *Figure 62*, it is evident that the predominant angle of the atomic lines in the moving image was badly detected and the fixed image doesn't fit to it.

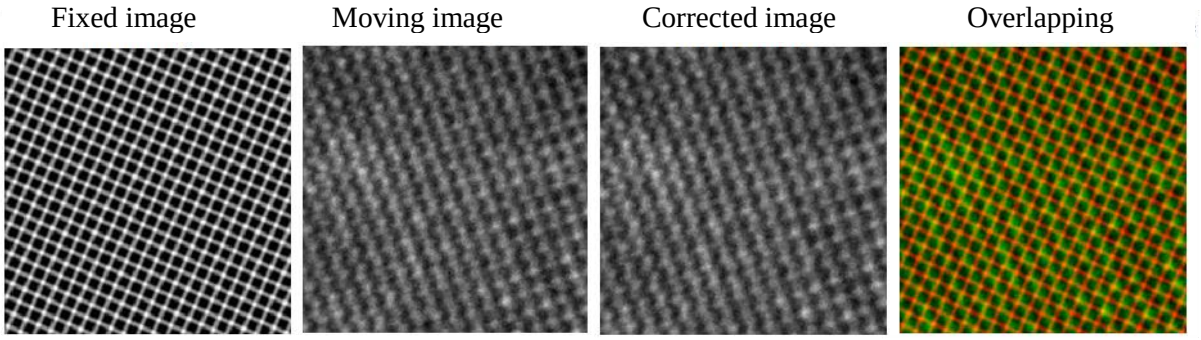

Figure 62: An exemple of mis-registration due to the bad initiation of fixed image

The explanation is in bad Fourier detection of the desirable angle representing the atomic lines. There are four main Bragg dots in the amplitude spectrum (red circles in *Figure 63*-a) representing the main angle of atomic lines (red line in *Figure 63*-b) and four secondary Bragg dots (yellow circles in *Figure 63*-a) representing the secondary angle (yellow line in *Figure 63*-b). According to the regular placements of the dots, it can be assumed that the red dots are indicative of the two perpendicular directions forming a square with a quartet of atoms and the yellow dots represent the diagonals between these atoms. The Matlab code works only with the first quadrant of the amplitude spectrum and detects the brightest dot. The yellow one (marked with * in *Figure 63*) was in this specific case detected as brighter than the red one (marked with ** in *Figure 63*). It is why the bad angle (representing the diagonal between atoms) was found.

In this case, the registration itself can do nothing more about it, because the optimization is strictly limited into the searched space and the rotation isn't allowed. A solution would consist in a simultaneous detection of the brightest dots in all four quadrants of the amplitude spectrum with the choice of the brightest dot in the end. It would considerably reduce the probability of selection of a wrong Bragg dot. Another option would be to process the spectrum of the whole image, not only the 256x256 px area.

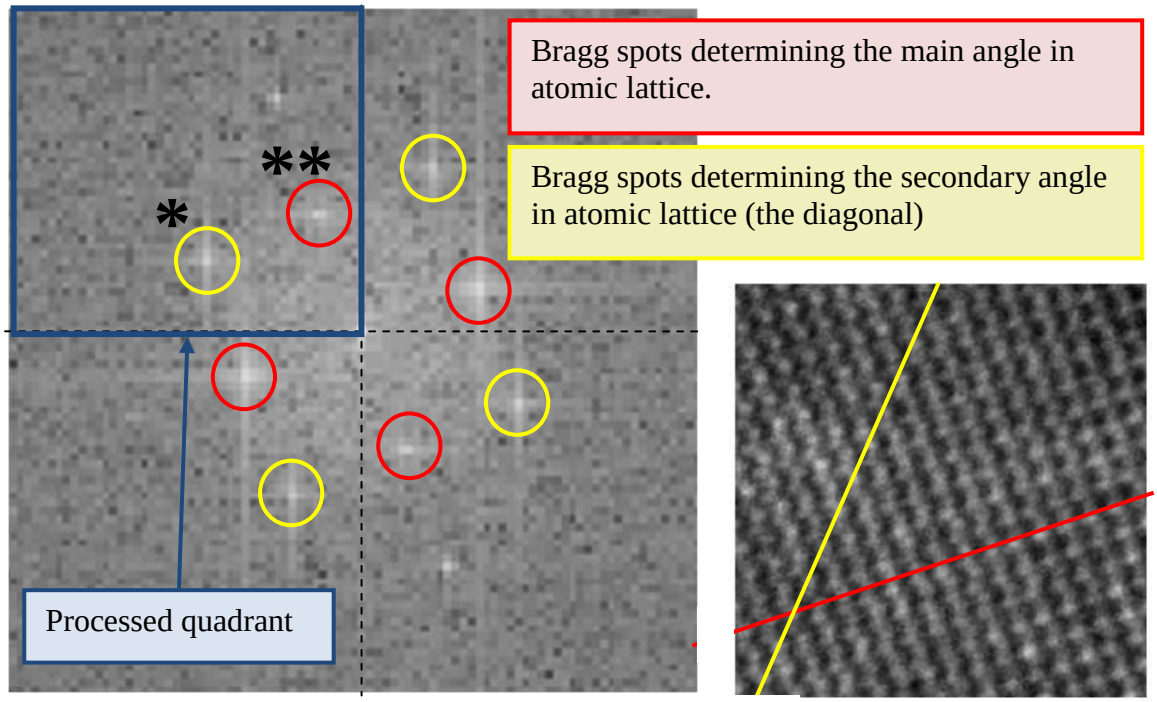

Figure 63: Angle detection from Amplitude spectrum

Low image quality

A moving image from *Figure 64* is affected by bad contrast and brightness. But more severe is that there is a big blurred area with very low quality (in red circle). There is a risk that if the sub-image used for the first run of registration is located in this area, so the first six coefficients are estimated completely wrong. The second run of optimization then continues in wrong direction and the local optimum can be reached. *Figure 64* shows that the registration is not successful due to all these factors (the corrected image is deformed by bad scale in the vertical direction).

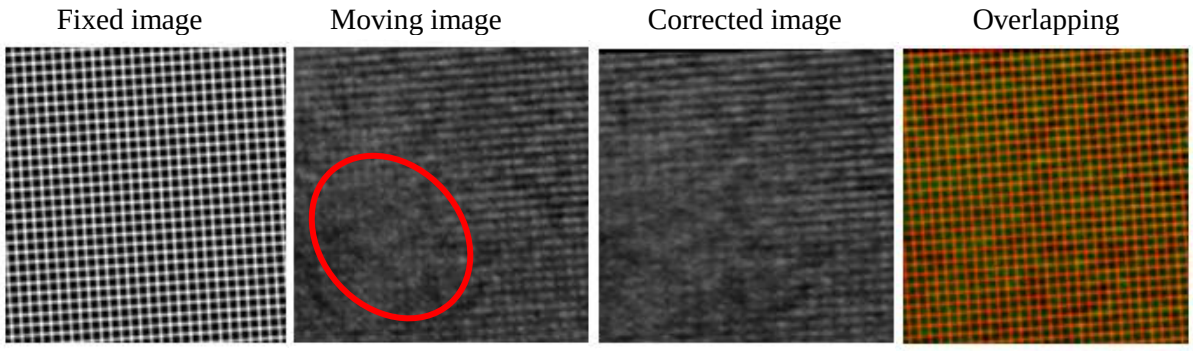

Figure 64: An example of mis-registered images

8 DISCUSSION

8.1 Evaluation of results

Concerning the results from the main set of images, the algorithm can be considered as successful. With the same registration parameters and the automatic run of the algorithm, the 97 % of images were corrected well. The evaluation was done using overlapping of the coloured layers (corrected image in green and fixed image in red). A big advantage is that the method is universal for images of all magnifications without the necessity of writing the value manually. The frequency of atomic lines is automatically estimated from the Fourier spectrum. The remaining 3 % of mis-registered images would be apparently corrected by adjusting the registration parameters or more simply by repeating the registration once or twice again. The algorithm is mostly a stochastic method so the bad result might be turned into the good one easily. Further work on the algorithm could exclude the block of Gradient descent because the improvement in quality is minimal compared to the Controlled random search. However, it depends on a concrete application. It was also proved, that the bi-level optimization used in this work saves considerably the time needed for the registration.

Concerning the results from the degraded images, there is a variety of results. In total, 70 % of images were registered well (mainly the images with visibly recognizable atoms). But the very noisy images were not. However, the bad results shouldn’t endanger the possible aplicability of the method, because there is an assumption of using a nice calibration standard (more in 8.4).

Concerning the optimization of parameters for the geometrical transformation, increasing the number of optimization cycles accompanied by the enlargement of the input population would certainly improve the process in terms of its quality. On the other hand, the time needed for calculation would be prolonged.

There is also a remark concerning the interpolation method. The cubic interpolation works well in terms of functionality of registration but the resulting image is slightly blurred. Better possibility would be to use the nearest neighbor interpolation method. Even it is the simplest interpolation method and the resulting image is not so smooth in appearance, it better preserves the frequency content and the image is more “comfortable” for observation by human’s eye. This problematics has been also discussed in [37].

8.2 Remark about criterion functions

Although the SSD was the main criterion function used for all testing in this work, the algorithm is universal for more criterion functions. There are four possibilities – SSD, CC, Cos and MI. There is an input parameter *k* in the algorithm which has values from 1 to 4 according to the chosen function (1-SSD, 2-CC, 3-Cos and 4-MI). The algorithm was tested on images of 90 px size with the same registration parameters for all functions. The results are in *Figure 65* (SSD, SS, Cos and MI). It is clear that the MI function doesn't give a good result. The problem is in very slow convergence to the optimum. So there was another testing with MI with modified registration parameters in order to achieve the convergence (shrinking of the population among the optimal solution) – the result is in *Figure 65* (MI 2). In this case, the input population size for *random generation search* was enlarged and the number of optimization cycles in both runs was almost doubled. The result is now comparable to those with SSD, CC and Cos, but the time for registration is extremely long (*Figure 66* - The blue columns represent successful registration and the red one represents mis-registration).

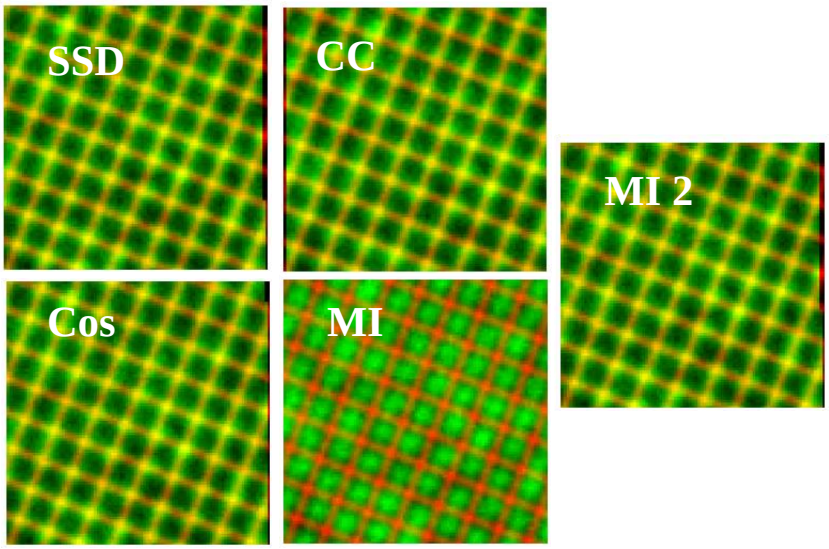

Figure 65: SSD, CC, Cos, MI – same registration parameters, MI 2 – adjusted parameters

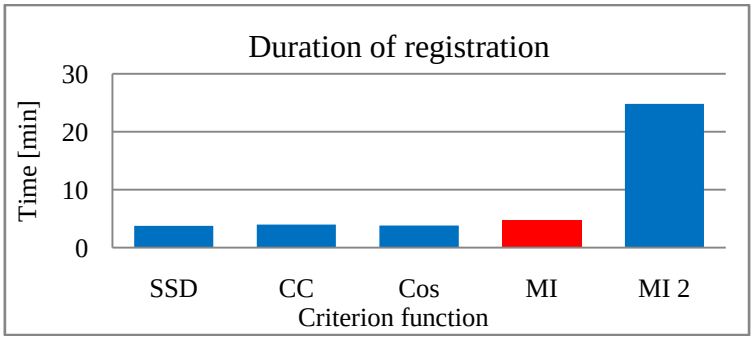

Figure 66: Time required for registration with different criterion functions.

8.3 Computational demands

The most time consuming base operation in the process of registration is the geometrical transformation. The new coordinates are calculated successively in *for* loop. Calculation of all new coordinates of an image of 256 px implies 256^2 iterations, so the time dependence on image size is quadratic. The subsequent interpolation doesn't take so long compared with that. Nevertheless, some time consumed by interpolation could be reduced by replacing the cubic interpolation by the nearest neighbour, as mentioned in chapter 8.1.

Average time needed to process an image of 256x256 px takes approx. 22 minutes in computer with processor Intel CORE i5 (2.3 GHz) with 4 GB RAM. The longest operation is the second optimization (CRS+SA) block which takes around 77% of total time (according to set conditions). The CRS+SA optimization block contains the geometrical transformation inside. Every iteration of the optimization also contains generation of a new individual (better than the worst one) – it means that there is a nested *while* loop that can increase the number of iterations. The nested loop generating a new point runs on average 4-5 times according to the observations. The geometrical transformation can be thus calculated 6 000 times during one optimization block of 1 500 iterations.

Time (and percentage) taken by individual blocks of registration are represented in *Table 5*. The percentages can vary with different registration parameters (number of iterations, image size etc.). Setting of these parameters must be done carefully with respect to the time requirements on one hand and the desired registration precision on the other hand.

Table 5: Time consumed by individual blocs of registration

Procedure	Time [s]	Percent %
Initiation of fixed image	0.4	0,03
1. run Random search	4.2	0,3
1. run CRS+SA (700 iterations, 60 px)	47.5	3,6
2. run Random search	67,6	5,2
2. run CRS+SA (1500 iterations, 256 px)	1000,1	76,7
Gradient (300 iterations)	185,6	14,2

An idea how to accelerate the computation consists of parallelization during registration. Some suitable *for* loops could be remade into *parfor* loops. *Parfor* uses multiple workers on local machine [Matlab help]. A limitation is that there is a requirement of completely independent iterations. It would therefore be a good solution for computation of the geometrical transformation but not for optimization itself. A further idea how to make the registration process quicker is to re-programme the whole algorithm in C language.

8.4 Applicability of the method

Nowadays, the usual distortion level associated with images from TEM is around 1 %. However, the scientists – especially metrologists – require a good precision for quantitative measurements and would prefer to have the distortion level close to zero. A software solution would certainly be valuable for them.

The distortion correction method proposed in this work is tuned on images of atoms of gold. The gold is also defined as calibration sample for High Magnification (HM) range. The concept of final idea is to create the correction matrix separately for different acquisition parameters only once and to use this data to correct the final user image on the given system. Similar approach has been also used for GPA method (3.1).

A way of software realization might be in a form of simple button in the user´s interface (UI) of the microscope. The image correction could be either applied automatically or by user. The process would have to be linked with an adjustment of the "measurement tool" in the UI in order to properly define magnification calibration factors.

Such a software solution might also bring some hardware changes in the microscope. Better software would allow doing some savings in the material used for the microscope's lenses. Also some parts formed by Ni-Fe or Co-Fe composites could be replaced by 4 and 16 times cheaper Fe material, respectively.

A similar approach was used for Scanning Electron Microscopes (SEM) – the method has been presented in article *Geometric correction of SEM images* [37].

CONCLUSION

The diploma thesis “Correction of image distortion of microscopic scene” was about a proposition and realization of a method using the unaided model-based image registration for correction of the crystalline images acquired by the TEM.

The first chapter presented the TEM, its construction, operating modes, image formation and crystalline specimens. The second chapter summarized the optical aberrations of the TEM with an accent on the geometrical distortion. The third chapter described three methods for correction of distortion and strain measurement – none of these methods used the image registration but another approaches. The fourth chapter presented the image registration theory, the geometrical transformations and the optimization methods.

The practical part contained a design of algorithm for the correction of distortion using Matlab interface. The proposed algorithm was described in chapter five. The algorithm created in Matlab was designed for correction of distortions up to the third order polynomial. It is why a nonlinear polynomial function of third order was used as a function for geometrical transformation. The distorted image was corrected by the process of the intensity-based image registration with the SSD criterion function. The distorted atomic lattice from TEM was in this process “aligned” to the model artificial lattice. The optimization method optimizing a population (of transformation parameters) proposed in this work is mainly stochastic. The optimization consisted of multiple steps. The initiation of population was realized as *Random population search*, the following main block as bi-level *Controlled random search* connected with *Simulated annealing* and the last step consisted of the *Gradient descent* method refining the solution. The cubic interpolation method was used for the geometrical transformation. As mentioned in discussion, the nearest neighbour interpolation method shoud be probably a better variant.

The sixth and seventh chapter were summarizing the performed testing and results on simulated and real data. The thesis was concluded by a discussion evaluating the results. In summary, the registration algorithm was successful in 97 % of the cases (with “nice” input images). The degraded images were well registered in 70 % of the cases. The chapter also discussed the computational demands and the possible applicability of the method. The method might be put into practice and become a standart part of a microscopic software after a further tuning with big input images. The algorithm should be preferably re-programmed into the C language in order to decrease the computational demands.

REFERENCES

[1] MALÍNSKÝ, Miloš a Ondřej SHÁNĚL. FEKT VUT BRNO, ÚBMI. *Úvod do elektronové mikroskopie: Přednáška z předmětu FMZT: Mikroskopická zobrazovací technika* [online]. 2015, 10-12-2015 [cit. 2015-12-25].

[2] SHÁNĚL O. Tolerances and misalignment aberrations for electron optical elements and systems. Brno: Vysoké učení technické v Brně, Fakulta strojního inženýrství, 2014. 87 s. Supervisor of doctoral thesis Ing. Jakub Zlámal, Ph. D.

[3] REIMER, Ludwig a Helmut KOHL. *Transmission electron microscopy: physics of image formation*. 5th ed. New York: Springer, 2008, XVI, 587 s. Springer series in optical sciences. ISBN 978-0-387-40093-8.

[4] RAY F. EGERTON. *Physical principles of electron microscopy an introduction to TEM, SEM, and AEM*. Corr. 3. print. New York: Springer Science Business Media, 2005. ISBN 978-038-7260-167.

[5] *Miller Indices presentation* [online]. Illinois Institute of Technology: Academic Resource Center [cit. 2015-12-26]. Dostupné z: https://web.iit.edu/sites/web/files/departments/academic-affairs/Academic%20Resource%20Center/pdfs/Miller_Indices.pdf

[6] *Contrast in TEM and STEM: Amplitude and Phase contrast* [online]. [cit. 2015-12-28]. Dostupné z: http://www.uio.no/studier/emner/matnat/fys/FYS4340/h13/lecture-notes/amplitude-contrast-and.ppt

[7] ZÁHORA, J., Š. LÝSKOVÁ a T. JAKUBEC. Difrakce elektronů v krystalech, zobrazení atomů. In:*Týden vědy* [online]. 2012 [cit. 2015-12-28]. Dostupné z: http://tydenvedy.fjfi.cvut.cz/2012/cd/prispevky/sbpdf/difrel.pdf

[8] ERNI, Rolf. *Aberration-corrected imaging in transmission electron microscopy: an introduction*. 2nd edition. Hackensack, NJ: Distributed by World Scientific Pub. Co., 2010, Chapter 7: Aberrations. ISBN 978-1-84816-536-6. Dostupné také z: http://www.worldscientific.com/doi/suppl/10.1142/p703/suppl_file/p703_chap07.pdf

[9] BRYDSON, Rik a Susan BROOKS. *Aberration-corrected analytical transmission electron microscopy: Appendix A: Aberration notation*. Hoboken, N.J.: Wiley, 2011, xv, 280 p., [8] leaves of plates. ISBN 9780470518519. Dostupné také z: http://onlinelibrary.wiley.com/doi/10.1002/9781119978848.app1/pdf

[10] HŸTCH, M.J., E. SNOECK a R. KILAAS. Quantitative measurement of displacement and strain fields from HREM micrographs. *Ultramicroscopy*. 1998, **74**(3): 131-146. DOI: 10.1016/S0304-3991(98)00035-7. ISSN 03043991.

[11] *GPA for DigitalMicrograph: Geometric Phase Analysis User Manual 4.5* [online]. 2015 [cit. 2015-10-25]. Dostupné z: http://www.hremresearch.com/Eng/download/documents/gpa4dm.pdf

[12] Extracting Quantitative Information from High Resolution Electron Microscopy, Kret, S.; Ruterana, P; Rosenauer, A. ;Gerthsen, D. physica status solidi (b), 2001, Vol.227(1), pp.247-295

[13] *PPA for DigitalMicrograph: Peak Pairs Analysis User Manual v3.2* [online]. 2015 [cit. 2015-10-25]. Dostupné z: http://www.hremresearch.com/Eng/download/documents/PPA%20Manual%20v3.2.pdf

[14] GALINDO, Pedro L., Sławomir KRET. The Peak Pairs algorithm for strain mapping from HRTEM images. *Ultramicroscopy*. 2007, **107**(12): 1186-1193. DOI: 10.1016/j.ultramic.2007.01.019. ISSN 03043991.

[15] KLEIN, Stefan, Marius STARING, Keelin MURPHY, Max VIERGEVER a Josien PLUIM. *Elastix: a toolbox for intensity-based medical image registration* [online]. [cit. 2015-11-21]. Dostupné z: http://elastix.isi.uu.nl/marius/downloads/2010_j_TMI.pdf

[16] ZITOVA, B., FLUSSER, J. Image Registration Methods: A Survey. *Image and Vision Computing*. 2003, vol. 21, no. 11, pp. 977-1000.

[17] ZITTOVÁ, B., FLUSSER, J. Image registration methods: a survey. Image and Vision Computing, Vol. 21, No. 11, pp. 977-1000, Oct 2003

[18] SEMMLOW, John L. *Biosignal and medical image processing*. 2nd ed. Boca Raton: CRC Press, 2009, 450 s. ISBN 978-1-4200-6230-4.

[19] *ITK: National Library of Medicine Insight Segmentation and Registration Toolkit* [online]. In: . [cit. 2015-11-21]. Dostupné z: https://ibia.umit.at/ResearchGroup/Phil/web/Simple2D3DRegistrationFramework.html

[20] JAN, J. *Medical Image Processing, Reconstruction and Restoration: Concepts and Methods*. Boca Raton: Taylor & Francis, 2006. ISBN 0-8247-5849-8, 730 s.

[21] WALBERG, George. *Geometric transformation techniques for digital images: a survey* [online]. DEPARTMENT OF COMPUTER SCIENCE, COLUMBIA UNIVERSITY. 1988 [cit. 2015-12-03]. Dostupné z: http://core.ac.uk/download/pdf/27291581.pdf

[22] RHODY, Harvey. *Geometric Image Transformations* [online]. Chester F. Carlson Center for Imaging Science Rochester Institute of Technology, 2005 [cit. 2015-12-03]. Dostupné z: https://www.cis.rit.edu/class/simg782/lectures/lecture_02/lec782_05_02.pdf

[23] *Neighborhood Operations*: Based on material from Digital Imaging: Theory and Applications.*www.viz.tamu.edu* [online]. 9-4-2000 [cit. 2016-01-02]. Dostupné z: http://www.viz.tamu.edu/faculty/parke/ends489f00/notes/sec1_8.html

[24] Bilinear interpolation. *Stackoverflow* [online]. 9-4-2000 [cit. 2016-01-02]. Dostupné z: http://stackoverflow.com/questions/28594316/i-want-to-use-bilinear-interpolation-to-calculate-the-summation-of-vectors

[25] PASCAL GETREUER, Linear Methods for Image Interpolation, *Image Processing On Line*, 1 (2011). DOI: 10.5201/ipol.2011.g_lmii

[26] MAES, F., COLLIGNON, A., VANDERMEULEN, D., et al. *Multimodality Image Registration by Maximization of Mutual Information*. IEEE Transaction on Medical Imaging, 1997, vol. 16, no. 2, pp. 187-198.

[27] PLUIM, J.P.W., MAINTZ, J.B.A., VIERGEVER, M.A., Mutual-Information-Based Registration of Medical Images: A Survey, IEEE Transactions on Medical Imaging, 2003, vol. 22, no. 8, pp. 986- 1004.

[28] MÉZL, M. a J. KOZUMPLÍK. VUT FEKT, ÚBMI. *Evoluční algoritmy: přednášky a materiály ke cvičením* [online]. Brno, 2015 [cit. 2016-01-01].

[29] XIAO-CHUN, Zou, Zhao XIN-BO a Feng YAN. An Efficient Medical Image Registration Algorithm Based on Gradient Descent. *2007 IEEE/ICME International Conference on Complex Medical Engineering*. IEEE, 2007, 636-639. DOI: 10.1109/ICCME.2007.4381814. ISBN 978-1-4244-1077-4

[30] PAZDERIN, Andrey, Sergey YUFEREV a Feng YAN. Power flow calculation by combination of Newton-Raphson method and Newton's method in optimization. *2009 35th Annual Conference of IEEE Industrial Electronics*. IEEE, 2009, 1693-1696. DOI: 10.1109/IECON.2009.5414826. ISBN 978-1-4244-4648-3.

[31] TVRDÍK, J. *Evoluční algoritmy*. skriptum VŠB-TU Ostrava, 2004

[32] PRICE, W. L. *A controled random search procedure for global optimisation*. The Computer Journal, Vol. 20, No. 1, pp. 367-370, Feb 1976

[33] AIT-AOUDIA, Samy a Ramdane MAHIOU. Medical Image Registration by Simulated Annealing and genetic algorithms. *Geometric Modeling and Imaging (GMAI '07)* [online]. IEEE, 2007, : 145-148 [cit. 2016-01-01]. DOI: 10.1109/GMAI.2007.25. ISBN 0-7695-2901-1.

[34] JOHANSSON, M. *Image Registration with Simulated Annealing and Genetic Algorithms*. Sweden, 2006. ISSN-1653-5715. Master's Thesis. Royal Institute of Technology. Vedoucí práce Lars Kjelldahl.

[35] LUCK, J., C. LITTLE a W. HOFF. Registration of range data using a hybrid simulated annealing and iterative closest point algorithm. In:*Proceedings 2000 ICRA. Millennium Conference. IEEE International Conference on Robotics and Automation. Symposia Proceedings (Cat. No.00CH37065)* [online]. IEEE, 2000, s. 3739-3744 [cit. 2016-04-11]. DOI: 10.1109/ROBOT.2000.845314. ISBN 0-7803-5886-4

[36] HAJNAL, Joseph V., D. J. HAWKES a Derek L. G. HILL. *Medical image registration*. Boca Raton: CRC Press, c2001. Biomedical engineering series (Boca Raton, Fla.). ISBN 08-493-0064-9.

[37] KAPUR, Jay P., David P. CASASENT a Andrew G. TESCHER. Geometric correction of SEM images. *Hybrid Image and Signal Processing VII.* 2000, 165-176. DOI: 10.1117/12.391928.